High-Frequency Electronics for Contactless Dielectrophoresis

John Lawrence Caldwell

Thesis submitted to the faculty of the Virginia Polytechnic Institute and State University
in partial fulfillment of the requirements for the degree of

Master of Science
In
Electrical Engineering

Rafael V. Davalos
Gary S. Brown
Kathleen Meehan

May 3, 2010
Blacksburg, VA

Keywords: Sample Enrichment, Dielectrophoresis, Electrorotation

High-Frequency Electronics for Contactless Dielectrophoresis

John Lawrence Caldwell

ABSTRACT

The field of sample enrichment is currently receiving a large amount of attention because it is essential to reduce the time required for many laboratory processes. Dielectrophoresis, or the motion of a polarized particle in the presence of a non-uniform electric field, has emerged as a promising method for biological sample concentration. By relying upon electrical properties that are intrinsic to a cell or microparticle, dielectrophoretic concentration avoids the need for sample preparation procedures which can greatly reduce the throughput of a system. Contactless Dielectrophoresis (cDEP) is a promising manifestation of dielectrophoresis in which the electrode structures that provide the non-uniform electric field are physically separated from the sample by a thin dielectric barrier.

This work presents two methods for providing the high-voltage and high-frequency signal necessary to generate a non-uniform electric field in the sample channel of a cDEP device. The first method, an oscillator-based system, was able to produce DEP trapping and pearl-chaining of THP-1 and MCF-7 breast cancer cells in a cDEP device. The second method presented here utilizes an amplifier and transformer combination to generate very high voltages over a wide range of frequencies. Finally, electrorotation, or the spin imparted to a particle due to a rotating electric field has proven to be an extremely useful analysis of a cell's dielectric properties. A wideband, computer controlled function generator, outputting four sinusoidal waveforms in quadrature is presented. This device was able to produce outputs with the proper alignment over the range of 10 Hz to 100MHz.

Acknowledgements

This work would not have been possible without the contributions of every member of the BioElectroMechanical Systems Laboratory at Virginia Tech. It is rare in life that one gets to work with such amazing people. I would especially like to thank my advisor Dr. Rafael Davalos for providing me with the opportunity to be a part of this research and for allowing me to pursue those wild ideas that make our lab unique. I would also like to thank my advisor in electrical engineering Dr. Gary Brown, whose guidance and support made it possible for me to pursue this research. To the members of the cDEP group, Hadi Shafiee, Mike Sano, and Erin Henslee, thank you for continuously inspiring me to be a better engineer and to push the limits of what I thought possible.

To my family, who has always supported me in every endeavor, even when it meant going to college, and then graduate school, on the other side of the country, there are no words to express my gratitude. This thesis is dedicated to my parents, Paul and Pam Caldwell, for their never-ending support of my ambitions.

All Photos by Author, 2010.

Table of Contents

Table of Figures

List of Tables

Chapter 1. Introduction

Efficient biological particle separation and concentration is a crucial issue in the development of integrated microfluidic systems for biomedical applications. This is because sensitive laboratory analysis procedures, especially those in the biomedical field, often require a concentration procedure before any analysis is performed. A multitude of sample enrichment techniques have arisen in order to meet this need, they include density gradient based centrifugation or membrane filtration [1], fluorescent and magnetic activated cell sorting (F/MACS)[2-4], and laser tweezers[5]. Although each of these techniques is unique in its inherent advantages and disadvantages, all are forced to compromise between high sample throughput and highly-specific isolation. The more selective of these techniques often require extensive sample preparation before being performed; relying upon prior knowledge of cell-specific markers and antibodies.

One alternative to these methods is dielectrophoresis (DEP) which is the motion of a particle due to its polarization in the presence of a non-uniform electric field [6, 7]. Traditionally, dielectrophoretic devices employ an array of thin-film interdigitated electrodes placed beneath fluid flowing in a microfluidic channel. This electrode array generates a non-uniform electric field that interacts with particles near its surface, often trapping them[8]. Such platforms have shown that DEP is an effective means to concentrate and differentiate cells rapidly and reversibly based on their size, shape, and intrinsic electrical properties. These intrinsic properties arise due to the membrane compositional and electrostatic characteristics, structure, and the type of nucleus associated with the cell type [9]. Unfortunately, the interdigitated electrodes employed by traditional DEP devices can require expensive and complicated fabrication procedures that are not well-suited for mass fabrication. Also, these electrodes are susceptible to fouling [10, 11] and may need to be coated with a passivation layer to prevent unwanted reactions with the sample fluid.

The BioElectricalMechanical Systems Laboratory at Virginia Tech has recently developed an alternative dielectrophoresis technique in order to address the problems commonly encountered in traditional dielectrophoretic devices. Contactless Dielectrophoresis (cDEP) forgoes the thin-film electrode array in favor of electrode reservoirs. These structures are filled with a conductive solution and placed adjacent to a microfluidic sample channel. The application of a time-varying signal to the electrode reservoirs causes their capacitive coupling to the sample channel where it induces an electric field. By varying the geometry of the electrode reservoirs, the sample channel, and insulating structures placed within the sample channe,l regions of relatively large DEP force have been demonstrated with the ability to concentrate target particles.

Contactless Dielectrophoresis has many advantages over traditional DEP devices. In terms of fabrication, two-dimensional cDEP devices can be produced using a single-mask soft-lithography process. Typically, cDEP devices are produced by first etching a master stamp from silicon and then using this stamp to mold devices from polydimethylsiloxane (PDMS). Using this technique, the sample channel and electrode reservoirs are produced in the same process, eliminating the need for multiple masks or thin film deposition. Furthermore, the need to apply a passivation layer to the electrodes is eliminated because the electrode reservoirs are already separated from the sample channel.

While the fabrication procedure for cDEP devices has been greatly simplified over traditional DEP devices, the electronics necessary for cDEP experimentation differ greatly from those that may be used with traditional DEP devices. The thin barrier of dielectric material between the electrode reservoirs and the sample channel exhibits a large impedance that must be overcome in order to induce an electric field in the sample channel. Overcoming this impedance requires the generation of electrical signals with both a high-frequency and high-voltage.

This work presents two approaches that have been used to produce the required signals for cDEP experimentation. The first approach is the use of a Royer oscillator circuit most commonly employed to drive the cold-cathode fluorescent lamps (CCFLs) used in the backlights of liquid-crystal displays. This approach facilitates the generation of high-voltage sinusoidal waveforms in a robust, compact and extremely inexpensive manner. A commercially available Royer oscillator circuit was used in the first demonstration of the cDEP technique where the system was successfully used to concentrate THP-1 human leukemia cells[12]. The second approach is the use of a wideband high-power amplifier whose output voltage is stepped-up by an accompanying transformer. Waveform generation is accomplished through the use of a standard laboratory function generator. This approach brings much greater flexibility in choosing the output waveform frequency and amplitude that is applied to the cDEP device. The increased flexibility of this approach has allowed the BioElectroMechanical Systems laboratory to demonstrate the use of cDEP to selectively isolate live cells from dead[13], and to concentrate THP-1 human leukemia cells as well as a wide range of synthetic microspheres[14].

Because both of these approaches represent a compromise between bandwidth, output amplitude, cost, and portability the selection of a signal generation technology is greatly dependant on the device's fabrication and the target particle to be isolated. With this in mind, the equipment to perform rotational spectroscopy of cells (ROT Spectra) has also been fabricated as a method to aid in both the design of cDEP devices and their associated signal generation electronics. A four-output quadrature sine wave generator was constructed exhibiting usable output amplitude from 10Hz to 100 MHz. The four independent signals were applied to a microelectrode array consisting of four gold electrodes deposited on a Pyrex wafer. By placing a sample of cells in the microelectrode array and mapping their rotation rate to the frequency and intensity of the applied electric field, the intrinsic electrical properties of the cell may be determined. Future cDEP devices may use this information to isolate a specific type of cell from a heterogeneous sample.

Chapter 2: Background

2.1 The Need for Sample Enrichment Techniques

The need to concentrate and enrich a biological sample has arisen in many areas of research. One such area of interest is pathogenic cell detection which is being pursued aggressively by several entities in order to ensure water and environmental quality[15], food safety[16], and clinical diagnosis[16]. Currently, the most popular analysis procedures used in pathogen detection include polymerase chain reaction (PCR), and culture and colony counting methods[16]. For environmental applications, these methods often rely on cultural enrichment to increase the number of targeted micro-organisms which may lengthen the process to several days[17]. These conventional methods are used despite their long turnover times because of their high selectivity and sensitivity. The fastest growing method of pathogen detection, biosensors, have the potential to shorten the time span between sample uptake and results, if they are able to reach selectivities and sensitivities comparable to established methods at significantly lower costs[16]. Indeed, the ultimate goal of pathogen detection research is to significantly reduce detection time.

The use of many rapid detection technologies could be expanded if targeted organism were separated, concentrated, and purified from the sample before detection[18]. This is because, in general, biological mixtures are complex, the concentrations of the compounds or cells of interest may be very low and the requirements for purity in sensitive analysis procedures are very high[19].

In order to meet the ever-present need for rapid, high-throughput, and selective pre-analysis enrichment, several techniques have been developed. The physical methods include: density gradient based centrifugation[20], membrane filtration[21], flow cytometry[22, 23], immunomagnetic separation[24], fluorescent and magnetic activated cell sorting(F/MACS) [2, 3, 25], and laser tweezers. Each of these techniques has inherent advantages and disadvantages and as of yet no technology has been developed that offers simple, rapid, and inexpensive enrichment of an organism from analysis inhibitors.

2.2 DEP as an Enrichment Technique

One alternative to these methods is dielectrophoresis (DEP) which is the motion of a particle due to its polarization in the presence of a non-uniform electric field[6, 7, 26, 27]. The term “dielectrophoresis” was created by Pohl in 1951 to describe the interaction between an electric field and a particle’s induced dipole. When a particle is exposed to an electric field, it polarizes creating a “dipole”; a term used in the analysis of electric fields to describe two equal charges of opposite polarity. If the dipole is placed in a non-uniform electric field, the forces acting on each of its component charges will not be equal and therefore a net force is created[28, 29]. Early forays into the field of DEP used machined needles to create the non-uniform electric field[30].

Current DEP devices typically employ an array of thin-film interdigitated electrodes patterned onto the surface of a substrate and placed under the flow of a sample channel. These electrodes generate a non-uniform electric field that interacts with the particles near the surface of the electrode array[31]. Previous work in this area has shown that this form DEP is an effective means to concentrate and differentiate cells rapidly and reversibly based on their size, shape, internal structure, and intrinsic properties such as conductivity and polarizability.

The application of DEP to separate target cells from a solution has been studied extensively in the last two decades. Examples of the successful use of DEP include the separation of human leukemia cells from red blood cells in an isotonic solution [32], the entrapment of human breast cancer cells from blood [33], and the separation of U937 human monocytic cells from peripheral blood mononuclear cells (PBMC) [34]. DEP has also been used to separate neuroblastoma cells from HTB glioma cells [34], isolate cervical carcinoma cells [35], isolate K562 human CML cells [36], separate live yeast cells from dead [37], and segregate different human tumor cells [38]. DEP has also proven an efficient, non-invasive method to characterize single cells, detect pathogens, and to manipulate viruses and macromolecules [26, 39-46].

Unfortunately, the interdigitated electrodes employed by traditional DEP devices can require expensive and complicated fabrication procedures that are not well-suited for mass production. Also, these electrodes are susceptible to fouling and may need to be coated with a passivation layer to prevent unwanted reactions with the sample fluid [10, 11].

Insulator-based dielectrophoresis (iDEP) was introduced as a practical method to obtain the selectivity of traditional DEP while overcoming its associated robustness issues[47]. iDEP relies on insulating obstacles rather than the geometry of its electrodes to produce spatial non-uniformities in the electric field. A simple iDEP device configuration is shown in Figure 1. One advantage of iDEP, is that the insulating structures typically traverse the entire depth of the channel and provide a non-uniform electric field over their entire depth, thus increasing the affected area. This advantage typically results in a higher throughput for the technique when compared to traditional DEP.

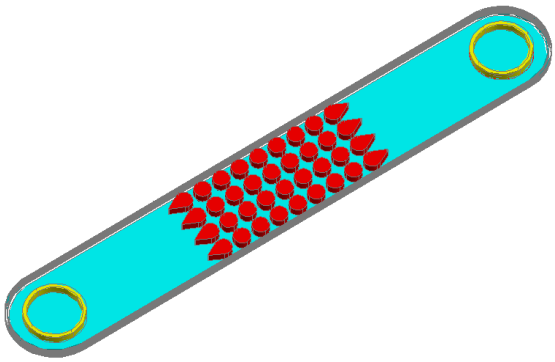

Figure 1: CAD drawing of an iDEP microfluidic device. The red pillars are insulating obstacles placed in the microfluidic channel (blue) to create non-uniformities in the electric field produced by the elctrodes at either end of the channel (yellow).

The basic concept of the iDEP technique was first presented by Masuda et al.[47]. Others have demonstrated with glass insulating structures and AC electric fields that iDEP can separate DNA molecules, bacteria, and hematapoietic cells[48]. It has been shown that polymer-based iDEP devices are effective for selective trapping of a range of biological particles in an aqueous sample[49]. iDEP technology has also shown the potential for water quality monitoring [50], separating and concentrating prokaryotic cells and viruses[51], concentration and separation of live and dead bacteria[52], sample concentration followed by impedance detection[53], and manipulation of protein particles[54].

The insulating obstacles employed by iDEP, meant to address the shortcomings of traditional DEP, are less susceptible to fouling than integrated electrodes[55]. In addition, the DC field used creates electrokinetic flow and moves the solution and particles through the device, alleviating the need for a pump to provide pressure-driven flow[49, 51]. iDEP's fabrication process is also much less complicated; the insulating obstacles can be patterned while etching the microchannel in one step. This technique has the added benefit of making the process more economical in that mass fabrication can be facilitated through the use of injection molding or hot embossing. However, like traditional DEP, iDEP is not without disadvantages. One of the primary drawbacks of an iDEP system is the presence of a high electric field intensity within the highly conductive biological fluid inside the microchannel [11, 56]. The combination of a large electric field across a conductive fluid causes joule heating and a dramatic temperature increase.

2.3 Contactless Dielectrophoresis

The ideal DEP technique would combine iDEP's simple fabrication process and resistance to fouling with DEP's reduced susceptibility to joule heating, all-the-while preserving the cell manipulation abilities of both methods. The BioElectricalMechanical Systems Laboratory at Virginia Tech has recently developed an alternative dielectrophoresis technique in order to address the problems commonly encountered in traditional dielectrophoretic devices. Contactless Dielectrophoresis (cDEP) forgoes the thin-film electrode array in favor of electrode reservoirs. As is shown in Figure 2 the electrode reservoirs (yellow) are filled with a conductive solution and placed adjacent to a microfluidic sample channel.

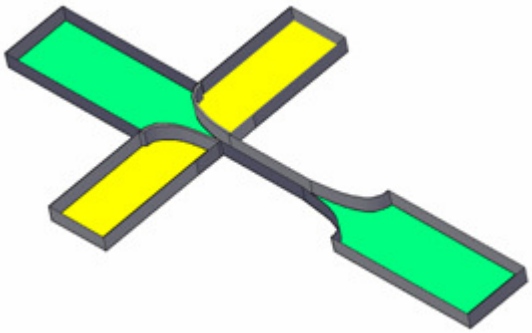

Figure 2: Cad drawing of the first device to demonstrate contactless dielectrophoresis.

The application of a time-varying signal to the electrode reservoirs causes their capacitive coupling to the sample channel (green) where it induces an electric field. By varying the geometry of the electrode reservoirs, the sample channel, and insulating structures placed within the sample channel regions of relatively large DEP force can be produced and have demonstrated with the ability to concentrate target particles.

Contactless Dielectrophoresis has many advantages over traditional DEP devices. In terms of fabrication, two-dimensional cDEP devices can be produced using a single-mask soft-lithography process. Typically, cDEP devices are produced by first etching a master stamp from silicon and then using this stamp to mold devices from polydimethylsiloxane (PDMS). Using this technique, the sample channel and electrode reservoirs are produced in the same process, eliminating the need for multiple masks or thin film deposition. Furthermore, the need to apply a passivation layer to the electrodes is eliminated because the electrode reservoirs are already separated from the sample channel.

While the fabrication procedure for cDEP devices has been greatly simplified over traditional DEP devices, the electronics necessary for cDEP experimentation differ greatly from those that may be used with traditional DEP devices. The thin barrier of dielectric material between the electrode reservoirs and the sample channel exhibits a large impedance that must be considered in the design of the associated electronics. Overcoming this impedance requires the generation of electrical signals with both a high-frequency and high-voltage.

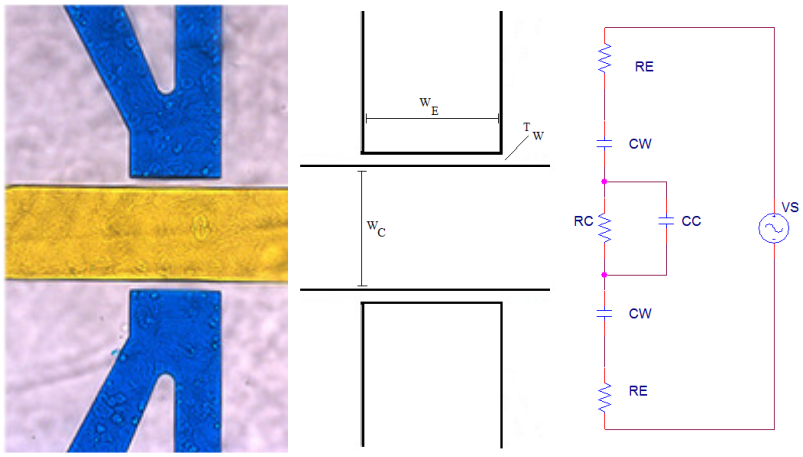

Figure 3: (Left) A cDEP device with its sample channel and electrode reservoirs highlighted with yellow and blue dyes respectively[14]. (Middle and Right) A simplified schematic of the cDEP device and the associated passive component model of the system.

This requirement of the signal generation equipment is easily described using a passive component model for an example cDEP device shown in Figure 3. The values of the passive components shown in the circuit model can be determined from the parameters shown in Table 1.

Table 1: Parameters of an example cDEP device used to determine a passive component model.

Parameter	Variable	Value	Unit
Electrode Length	L_E	.01	m
Electrode Width	W_E	200	μm
Electrode Depth	D_E	50	μm
Electrode Conductivity	σ_E	1.4	S/m
Channel Wall Thickness	T_W	20	μm
Channel Width	W_C	200	μm
Channel Conductivity	σ_C	.01	S/m
Channel Permittivity	ε_C	$80\varepsilon_0$	F/m
Substrate Permittivity	ε_W	$2.65\varepsilon_0$	F/m

Using the parameters in Table 1, realistic values for the components in the passive circuit model can be determined:

$$R_E = \frac{L_E}{\sigma_E W_E D_E} = \frac{.01m}{\left(\frac{1.4S}{m}\right)(200\mu m)(50\mu m)} = 714.3k\Omega \tag{3.1}$$

$$R_C = \frac{W_C}{\sigma_C W_E D_E} = \frac{200\mu m}{\left(\frac{.01S}{m}\right)(200\mu m)(50\mu m)} = 2M\Omega \tag{3.2}$$

$$C_W = \frac{\varepsilon_W W_E D_E}{T_W} = \frac{(2.65)(8.854 \times 10^{-12})(200\mu m)(50\mu m)}{(20\mu m)} = .012pF \tag{3.3}$$

$$C_C = \frac{\varepsilon_C W_E D_E}{W_C} = \frac{(80)(8.854 \times 10^{-12})(200\mu m)(50\mu m)}{(200\mu m)} = .035pF \tag{3.4}$$

From the above values it can be seen that the channel wall capacitance is a very small value. The passive component model allows the system to be modeled as a voltage divider with the voltage across R_C being proportional to the electric field intensity in the channel:

$$V_{RC} = V_S \frac{R_C || Z_{CC}}{2R_E + 2Z_{CW} + R_C || Z_{CC}} \tag{3.5}$$

Where || indicates two components connected in parallel and Z_{CW} and Z_{CC} are the impedances of the system capacitances whose magnitudes are defined as:

$$|Z_C| = \frac{1}{2\pi f C} \tag{3.6}$$

These values for a passive component model were then inserted into a PSpice model of the system and the device was simulated over a range of 100 Hz to 100 MHz with a 100Vrms AC source. The resulting voltage drop across the sample channel, which is proportional to the electric field intensity, is shown in Figure 4.

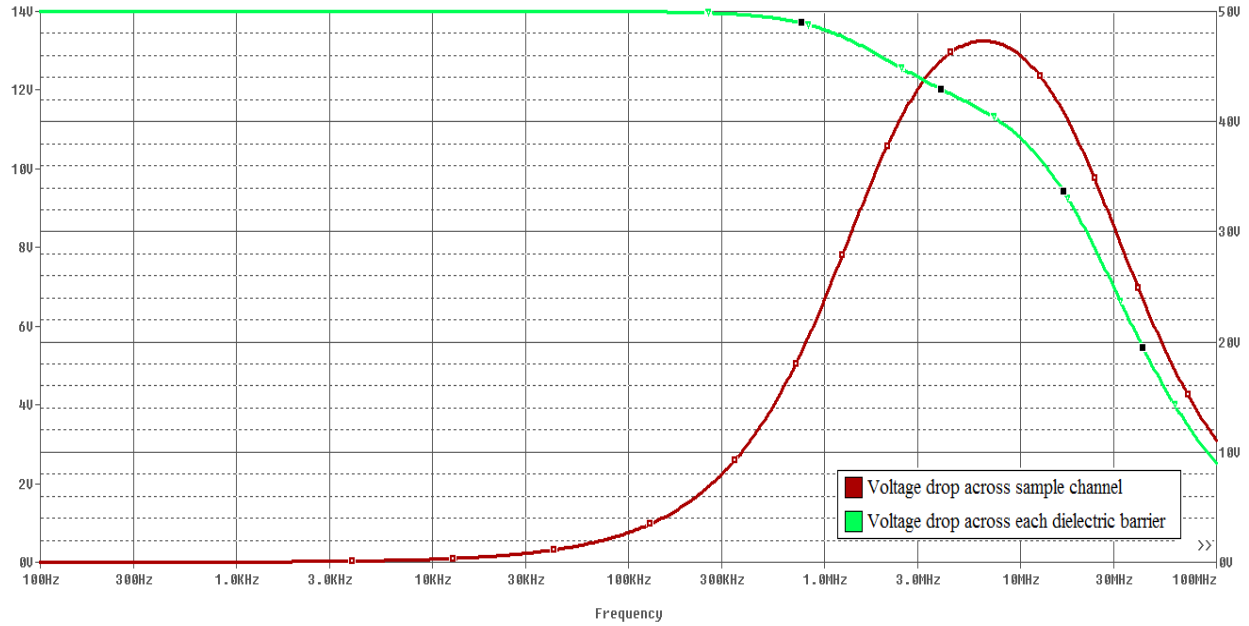

Figure 4: The voltage drop across the sample channel and a single dielectric barrier of a cDEP device with a 100Vrms source as a function of frequency.

Figure 4 illustrates that for the entire frequency, range the majority of the source voltage is dropped elsewhere in the system and not across the sample channel; thus necessitating a much higher voltage than conventional DEP devices.

While the passive component model of a cDEP device is a useful strategy for predicting the electric field intensity, it is not an accurate method of predicting the current the voltage source will be required to supply. This is because parasitics in the system, namely capacitances, will draw a much larger current than the microfluidic device itself.

2.4 Electrorotation Spectroscopy

Figure 4 in the previous section highlights that the electric field intensity in the sample channel of a cDEP device is highly dependent on frequency of the applied signal and the geometry of the device itself. As will be shown in detail in Chapter 3, the DEP force experienced by a cell or microparticle is also highly dependent on frequency. In fact, two different cells in the same non-uniform electric field may experience DEP forces of differing magnitude and direction. These differences arise from differing electrical properties of the cells themselves. If cDEP devices are to be used to enrich a target particle from a solution, their geometry must allow for a significant gradient of the electric field at frequencies coinciding with a high DEP response from the particle.

One method of determining the electrical properties of a cell or particle, and thus its DEP response, is through electrorotation spectroscopy. The term "electrorotation" is used to describe the spin of a polarized particle in a rotating electric field. By mapping the particle's rotation rate to the frequency of the applied field, a process known as electrorotation spectroscopy or ROT spectra, one gains insight into the electrical properties of the cell. ROT spectra may provide valuable information towards optimizing a cDEP device's geometry and by extension the DEP response on the particle of interest.

Electrorotation as a phenomenon has been observed throughout the entire history of dielectrophoretic experimentation including some of Pohl's earliest work[28]. However, the ability to extract meaningful information from this phenomenon was not immediately apparent. In 1982, Arnold and Zimmerman first showed there was a direct relationship between the rate of rotation of a plant protoplast and the applied electric field intensity[57]. In the same year they used the phenomenon to determine the membrane capacitance of Mesophyll cells[58]. This led to the use of rotating fields for cellular measurements by other groups [59, 60].

Up to this point it had not been clear why the cell rotation was in the reverse direction to the field rotation, or why co-field rotation occurred at extremes of the frequency spectrum[61]. Fuhr was the first to consider multi-shelled models of cells and show that the complexity of the rotation spectrum increased with the number of cellular layers[62]. A final advancement to the model of cells in a rotating field came when it was determined that the very thin plasma membrane can become dominant in the rotational spectrum of the cell[63], which led to the single shell cellular model derived in Chapter 3. This conclusion has also been verified through the electrorotation of liposomes[64]. The field of electrorotation has found many applications in the biomedical engineering field. These include its use to detect apoptosis in cells[65], the detection of variations in cell lines[66], and to determine the dielectric properties of single cells including yeast and red blood cells[67, 68].

Perhaps most important to the topic of this document is the techniques use as a design aid for dielectrophoretic sample enrichment systems. In 1994 Gascoyne et. al. published a rigorous study of the sensitivity of ROT spectra measurements to the variation of several experimental

parameters[69]. Because DEP and ROT spectra are complex, non-linear functions of a particle's dielectric properties and the experimental conditions, the most popular method of deducing particle dielectric properties is through curve-fitting methods such as the Nelder-Mead simplex optimization procedure[69]. The group was able to determine several conclusions in order to maximize the accuracy of dielectric parameters produced by ROT spectra measurements. First, for the single-shell dielectric model, each peak in the rotational spectrum can be used to determine uniquely two parameters. Also, if the DEP crossover frequency can be constrained in the numerical optimization, all five variables in the single-shell dielectric model can be determined. Finally, the frequency spectrum should be taken to as high a value as possible in order to encompass the co-field rotation peak[69]. By performing a sensitivity analysis of the experimental parameters involved with ROT spectra this group paved the way for the technology to aid in the design of dielectrophoretic sample enrichment devices.

An excellent example of this concept was published in 1999 by Yang et. al. in which the dielectric properties of human leukocyte subpopulations were determined through electrorotation and the feasibility of DEP to sort these cells was examined[70]. Using rotation rates measured at frequencies from 1 kHz to 120 MHz, the group was able to use a MATLAB-based curve fitting routine to extract the dielectric properties in the single shell model. From this information, a simulated DEP spectra was created showing four distinct DEP crossover frequencies for the four distinct cell types. This technique was later used by Gascoyne to design a DEP-based sample enrichment system to separate cancer cells from blood[41].

2.5 cDEP Device Fabrication

One of the main advantages of the cDEP technique is the fabrication process that is used to produce the devices. The process described here has been used to produce devices for several publications and is based upon a "stamp and mold" process incorporating a single-mask photolithographic process[12-14]. A silicon master stamp is fabricated on a <100> silicon substrate by first spinning photoresist onto the wafer (AZ 9260, AZ Electronic Materials) and soft baking at 114°C for 45 s(Figure 5(a)). The wafer is then exposed to UV light for 45 s with an intensity of 12 W/m through a chrome-plated glass mask. The exposed photoresist is removed using Potassium-based buffered developer AZ400K followed by another hard baking at 115°C for 45 s(Figure 5(b)). Deep Reactive Ion Etching (DRIE) is used to etch the silicon master stamp to depths ranging from 50-100 microns(Figure 5(c)). The silicon master stamp is then cleaned with acetone to remove any remaining photoresist(Figure 5(d)). The scalloping effect, a typical effect of the DRIE etching method, creates a surface roughness which is detrimental to the stamping process. In order to reduce the surface roughness, silicon oxide is grown on the silicon master using thermal oxidation and then removed. The results of this process can be seen in Figure 5(h-i).

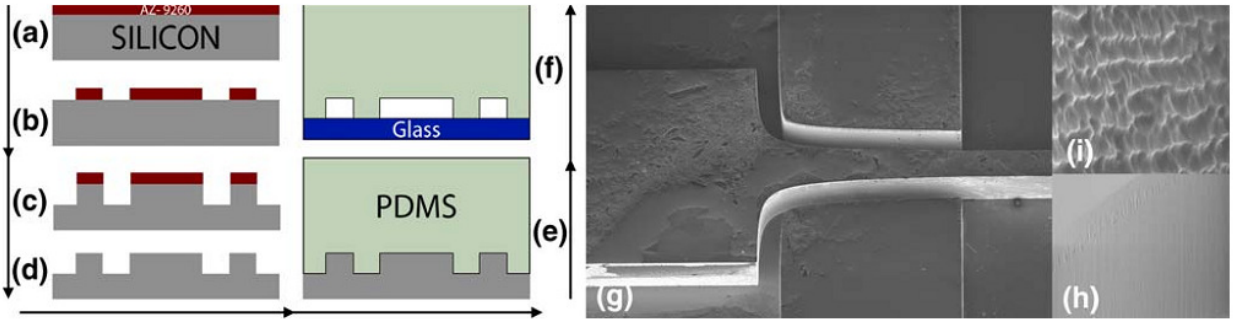

Figure 5: (a-f) Process flow used to fabricate cDEP devices by employing photolithography. (g) SEM images of the silicon wafer mold at the interestion of the sample channel and electrode reservoirs of the device (h) Reduced surface roughness of the wafer after the growth and removal of an oxide layer. (i) Surface scalloping as a result of the DRIE process[12].

A mold of the master stamp is then made using PDMS. Liquid phase PDMS is made by mixing the PDMS monomers and the curing agent in a 10:1 ratio (Sylgrad 184, Dow Corning, USA). Bubbles in the liquid PDMS are removed by exposing the mixture to vacuum for an hour. The clean PDMS liquid is then poured onto the silicon master and allowed to de-gas for 15 minutes. The PDMS is then cured for 45 min at 100°C (Figure 5(e)) and removed from the stamp. Fluidic connections to the channels are punched with 15 gauge blunt needles (Howard Electronic Instruments, USA). The PDMS mold is then bonded to a glass microscope slide to form a functioning fluidic device using air plasma. A completed cDEP microfluidic device is shown in Figure 6 with its sample channel and electrode reservoirs illuminated by a fluorescent fluid.

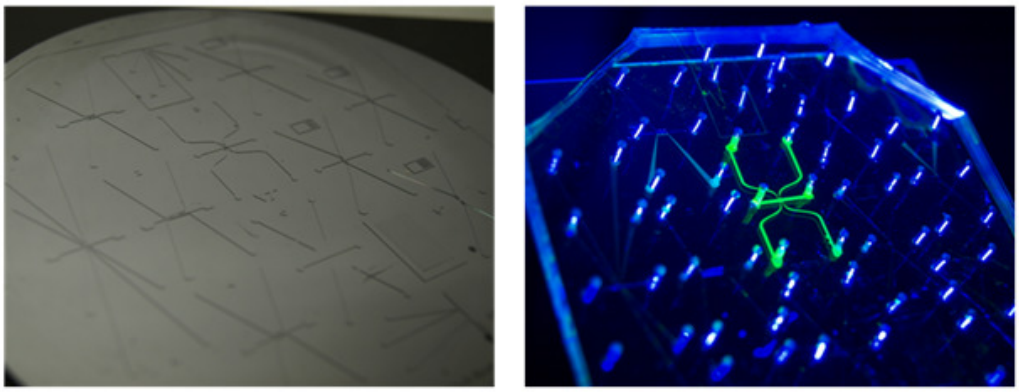

Figure 6: (Left) A silicon wafer with a large number of prototype designs etched into its surface using DRIE. (Right) A completed cDEP device. The channels of this device have been filled with a fluorescent fluid and the device is exposed to 400 nm UV light to aid in visualization.

Once the PDMS mold has been bonded to the glass microscope slide fluidic and electrical connections can be made to the device. An example system configuration is shown in Figure 7 where a pressure driven flow is provided in the sample channel by a syringe pump. Electrical connections are made by first filling the electrode reservoirs with a highly conductive fluid and then inserting wire electrodes into the holes punched in the PDMS.

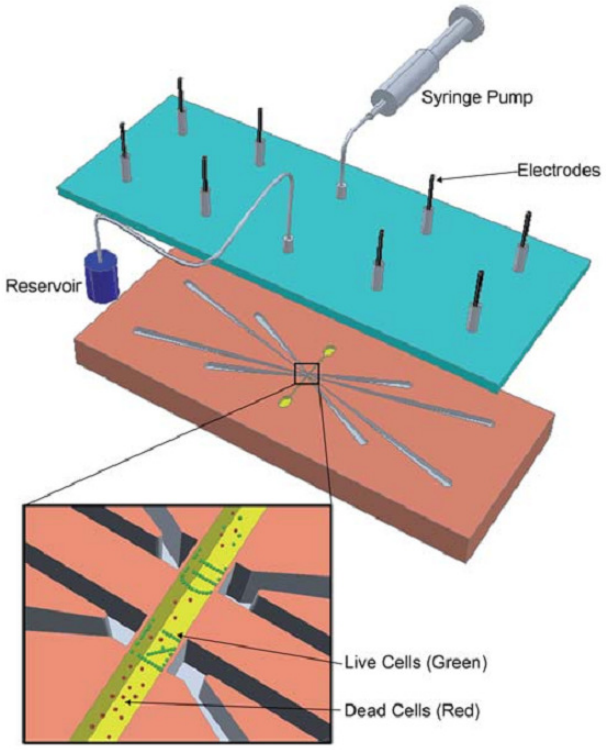

Figure 7: An example system configuration for cDEP experimentation. Fluidic and electrical connections are made through the holes punched in the PDMS[13].

There are several advantages to this process. First, the silicon master stamp is the only portion of the process that must be performed in a clean room using photolithography. Once the stamp has been produced, the devices can be replicated outside of the clean room and the stamp can be used multiple times. Another advantage of this process is that cDEP devices tend to be small compared to the size of a standard 10 cm silicon wafer. Therefore a multitude of designs can be prototyped and fabricated at the same time, on the same wafer, using a single mask. A silicon wafer with a large number of devices is shown in Figure 6.

2.6 Electrical Safety

Due to the high-voltages necessary for cDEP experimentation, electrical safety was of paramount concern. To start, all experiments described in this document were performed with a microscope that was enclosed in a metal cage connected to the building safety ground. This was done to ensure that an electrical arc formed during an experiment would be conducted to ground away from the microscope user. All electronics used for the generation of electric fields for cDEP devices feature a connection to monitor the output signal such that the user always is aware of the system's state and output voltage. In the case of the oscillator-based system, all electronics were enclosed in a non-conductive plastic case with a large "high voltage" warning on the outside of the enclosure. This configuration ensures that if the enclosed electronics made accidental contact with the case, the user would not receive an electrical shock. The high-voltage transformer used in the amplifier-based system is enclosed in a metal chassis that is connected to the building safety ground. Finally, all connections in the system above signal-level are made using custom high-voltage wiring. Despite all safety measures employed, high-voltage experiments require caution and attentiveness to the state of the system at all times.

Chapter 3. Theory

The force and torque imparted to a cell or biological particle in a suspending medium due to a non-uniform electric field are derived here using the effective dipole moment method [71]. This method assumes that the cell can be approximated as a lossy dielectric sphere whose length scale is small compared to the non-uniformity of the electric field.

3.1 The Effective Dipole Moment

An electric dipole is the name given to two point charges of equal magnitude and opposite sign, separated by a distance which is small compared to the distances at which we wish to know the potential field. Consider the dipole consisting of two point charges of charge "Q" separated by a vector of length "d":

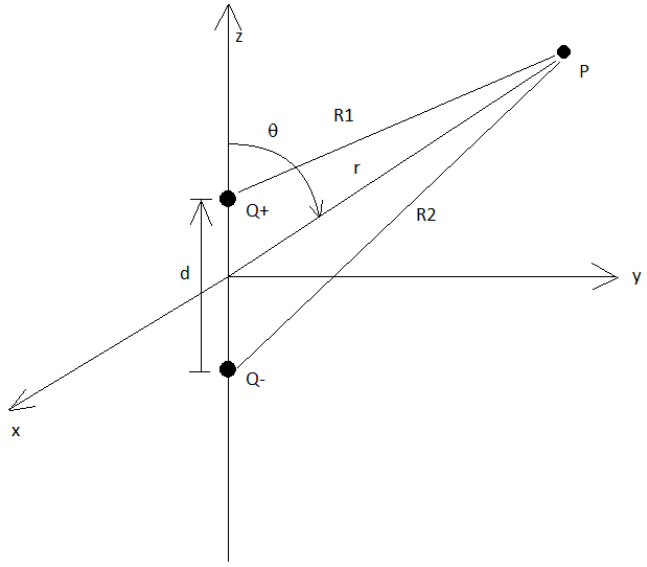

Figure 8: A dipole composed of two point charges places on the z-axis. Arbitrary point P is used to derive the potential field of the dipole.

The electrostatic potential at the point P can be determined by adding the scalar potentials of the two charges, letting the distance from Q+ and Q- to point "P" be R_1 and R_2 respectively. The potential can then be written as:

$$\Phi = \frac{Q}{4\pi\varepsilon_O}\frac{R_2 - R_1}{R_2 R_1} \tag{3.1}$$

Where ε_O is the permittivity of free space. We also define a vector from the midpoint between the two charges to the point P: $\vec{r}$. For a distant point, $R_2 \approx R_1$ and therefore the product of the two vectors in the denominator may be replaced by r^2. The numerator may also be approximated at a distant point by assuming that R_1 and R_2 are parallel. This allows:

$$R_2 - R_1 = d\cos\Theta \tag{3.2}$$

The potential field from the dipole may be written in spherical coordinates:

$$\Phi = \frac{Q}{4\pi\varepsilon_O}\frac{d\cos\theta}{r^2} \tag{3.3}$$

The potential field is further simplified by using the dipole moment. If a vector length $\vec{d}$ is directed from Q- to Q+ then the dipole moment is:

$$\vec{p} = Q\vec{d} \tag{3.4}$$

Using the fact that $cos\theta = d \cdot \frac{\vec{r}}{|\vec{r}|}$, the electrostatic potential due to the dipole can be written as:

$$\Phi = \frac{\vec{p} \cdot \vec{r}}{4\pi\varepsilon_0 r^3} \tag{3.5}$$

Where $r = |\vec{r}|$. If we now add an electric field $\vec{E}$ equations for force and torque on the dipole may be determined. The force on a point charge "Q" from an electric field is defined as:

$$\vec{F} = Q\vec{E} \tag{3.6}$$

By summing the forces on the individual point charges of the dipole, the net force on the dipole can be written as:

$$\vec{F} = Q\vec{E}\left(\frac{d}{2}\right) - Q\vec{E}\left(\frac{-d}{2}\right) \tag{3.7}$$

The dipole approximation of force can be found through use of a Taylor series and taking the limit as $\left|\vec{d}\right| \to 0$:

$$\vec{F} = Q\vec{d} \cdot \nabla\vec{E} = \vec{p} \cdot \nabla\vec{\mathrm{E}} \tag{3.8}$$

The torque on the dipole due to electric field $\vec{E}$ around the midpoint between the charges can also be shown as:

$$\vec{T} = \frac{\vec{d}}{2} \times Q\vec{E} + \frac{\vec{d}}{2} \times (-Q)\vec{E} = \vec{p} \times \vec{E} \tag{3.9}$$

It is important to notice that in a uniform electric field, the net force on the dipole is zero because $\nabla\vec{\mathrm{E}} = 0$. However, there will be a net torque in a uniform electric field due to the opposite polarity of the charges.

Rather than two point charges, we now consider a dielectric sphere of radius "R" and permittivity ε_p suspended in an isotropic dielectric medium of permittivity ε_m and in an electric field $\vec{E}$. This field will have the effect of polarizing the sphere, causing a perturbation of the field which can be expressed as an induced electrostatic potential having the form[71]:

$$\Phi_{induced} \approx \frac{(\varepsilon_p - \varepsilon_m)R^3\vec{E} \cdot \vec{r}}{(\varepsilon_p + 2\varepsilon_m)r^3} \tag{3.10}$$

By setting equations 3.5 and 3.7 equal to each other an "effective dipole moment" of the dielectric sphere can be determined:

$$\vec{p}_{eff} = 4\pi\varepsilon_m K R^3\vec{E} \tag{3.11}$$

Where K = $(\varepsilon_p - \varepsilon_m)/(\varepsilon_p + 2\varepsilon_m)$ and is known as the Clausius-Mossotti factor. Equation 3.11 defines the moment of the equivalent electric dipole that would create a perturbation of the electric field identical to the dielectric sphere for all $|\vec{r}| > R$[71]. This is useful because the previously determined equations for force and torque on the dipole can now be applied to the dielectric sphere. Thus the DEP force on a lossless dielectric particle in a non-uniform electric field is determined by substituting equation 3.11 into equation 3.8 and employing the relationship: $\vec{E} \cdot \nabla\vec{E} = \frac{1}{2}\nabla\left|\vec{E}\right|^2$:

$$F_{DEP} = 2\pi\varepsilon_m K R^3 \nabla\left|\vec{E}\right|^2 \tag{3.12}$$

If this process is repeated to determine the torque from a non-uniform field:

$$\vec{T} = 2\pi\varepsilon_m K R^3\left(\vec{E} \times \vec{E}\right) = 0 \tag{3.13}$$

Equation 3.13 indicates that losses must be included in our model to accurately predict the torque on a cell resulting from a non-uniform electric field.

3.2 Particles with Concentric Shells

The development of the effective dipole moment method to determine force and torque is only valid if a more appropriate model of the target particle is used. Biological cells generally consist of multiple structures suspended in the cytoplasm and enclosed by a cell membrane. This section will define the Clausius-Mossotti factor and effective dipole moment for a dielectric sphere with a concentric shell and conductive losses.

In order to develop a more robust effective dipole model for the cell, we first consider a lossless dielectric sphere consisting of an inner shell of radius R_1 and permittivity ε_1, and an outer shell of radius R_2 and permittivity ε_2 as shown in Figure 9.

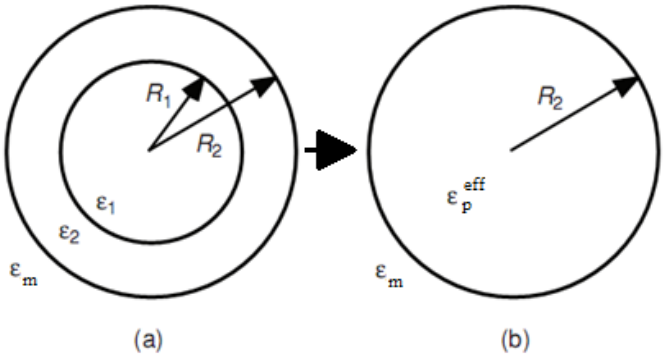

Figure 9: Transformation of multilayered particles: (a) a spherical particle containing an internal concentric shell (b) an equivalent homogeneous particle.

This sphere may be transformed into an equivalent homogeneous particle of radius R_2 through an examination of the external induced electrostatic potential function as was performed in the previous section[71]. The effective permittivity of the sphere is:

$$\varepsilon_p{}^{eff} = \varepsilon_2 \left\{ \frac{\left[\left(\frac{R_2}{R_1}\right)^3 + 2\left(\frac{\varepsilon_1 - \varepsilon_2}{\varepsilon_1 + 2\varepsilon_2}\right) \right]}{\left[\left(\frac{R_2}{R_1}\right)^3 - \left(\frac{\varepsilon_1 - \varepsilon_2}{\varepsilon_1 + 2\varepsilon_2}\right) \right]} \right\} \tag{3.14}$$

The effective induced dipole moment of the sphere is determined by substituting the above effective permittivity into the Clausius-Mossotti factor. However, in order to accurately model a biological cell, ionic charge conduction mechanisms within the cell as well as dielectric losses must be included in the model. Because these losses are frequency dependant, so must be the force and torque on the cell. Assuming that both the suspension medium and the particle are homogeneous dielectrics with ohmic electrical conductivities σ_p and σ_m respectively, their permittivities now become complex quantities:

$$\varepsilon_p{}^* = \varepsilon_p + \frac{\sigma_p}{j\omega} \tag{3.15}$$

$$\varepsilon_m{}^* = \varepsilon_m + \frac{\sigma_m}{j\omega} \tag{3.16}$$

Where ω is the radial frequency of the field and $j = \sqrt{-1}$. $\varepsilon_p{}^{*eff}$ is found by applying this concept to the effective permittivity of a sphere containing a single concentric shell found in equation 3.14:

$$\varepsilon_p{}^{*eff} = \varepsilon_2{}^* \left\{ \frac{\left[\left(\frac{R_2}{R_1}\right)^3 + 2\left(\frac{\varepsilon_1{}^* - \varepsilon_2{}^*}{\varepsilon_1{}^* + 2\varepsilon_2{}^*}\right) \right]}{\left[\left(\frac{R_2}{R_1}\right)^3 - \left(\frac{\varepsilon_1{}^* - \varepsilon_2{}^*}{\varepsilon_1{}^* + 2\varepsilon_2{}^*}\right) \right]} \right\} \tag{3.17}$$

Hence, the frequency-dependant Clausius-Mossoti factor will now be of the form:

$$K(\omega) = \frac{\varepsilon_p{}^{*eff} - \varepsilon_m{}^*}{\varepsilon_p{}^{*eff} + 2\varepsilon_m{}^*} \tag{3.18}$$

Finally, the effective dipole moment of the single shell particle with conductive losses is:

$$\vec{p}_{eff} = 4\pi\varepsilon_m K(\omega) R^3 \vec{E}_0 \tag{3.19}$$

Where $\vec{E}_0$ is a non-uniform electric field with sinusoidal time-variation.

3.3 Particles with Thin Shells

The complex effective permittivity of the particle found in the previous section may be simplified. To start, if we review the two radii of the sphere in Figure 9:

$$R_2 = R_1 + \delta \text{ and } \delta \ll R_2 = R \tag{3.20}$$

One may define capacitance and conductance per unit area of the membrane as:

$$C_\mu = \frac{\varepsilon_2}{\delta} \tag{3.21}$$

$$g_\mu = \frac{\sigma_2}{\delta} \tag{3.22}$$

These quantities allow the simplification of equation 3.17 to the following:

$$\varepsilon_p{}^{*eff} = \frac{C_\mu{}^* R \varepsilon_m{}^*}{C_\mu{}^* R + \varepsilon_m{}^*} \tag{3.23}$$

$$C_\mu{}^* = C_\mu + \frac{g_\mu}{j\omega}$$

3.4 Dielectrophoresis

The previously-derived effective dipole moment for a thin-shelled, lossy, dielectric particle can now be applied to determine the dielectrophoretic force acting on a biological cell. To start, equation 3.18 can be placed in Debye relaxation form:

$$K(\omega) = K_\infty + \frac{K_0 - K_\infty}{j\omega\tau_{MW} + 1} \tag{3.24}$$

$$K_\infty = (\varepsilon_p - \varepsilon_m)/(\varepsilon_p + 2\varepsilon_m)$$

$$K_0 = (\sigma_p - \sigma_m)/(\sigma_p + 2\sigma_m)$$

$$\tau_{MW} = (\varepsilon_p + 2\varepsilon_m)/(\sigma_p + 2\sigma_m)$$

τ_{MW} is the dipolar Maxwell-Wagner relaxation time for an ohmic dielectric sphere suspended in a similar medium. The Clausius-Mossotti factor to be separated into its real and imaginary parts[72]:

$$Re[K(\omega)] = \frac{(\sigma_p - \sigma_m)}{(1 + \omega^2\tau_{MW}^2)(\sigma_p + 2\sigma_m)} + \frac{\omega^2\tau_{MW}^2(\varepsilon_p - \varepsilon_m)}{(1 + \omega^2\tau_{MW}^2)(\varepsilon_p + 2\varepsilon_m)} \tag{3.25}$$

$$Im[K(\omega)] = \frac{3\omega\tau_{MW}(\varepsilon_p\sigma_m - \varepsilon_m\sigma_p)}{(1 + \omega^2\tau_{MW}^2)(\varepsilon_p + 2\varepsilon_m)(\sigma_p + 2\sigma_m)} \tag{3.26}$$

Equation 3.12 can now be updated to include the complex permittivies of the particle and medium:

$$F_{DEP} = 2\pi\varepsilon_m Re[K(w)]R^3\nabla\left|\vec{E}\right|^2 \tag{3.27}$$

A very important concept that can be used for particle separation is that at the frequency where $Re[K(w)] = 0$ there will be no force on the particle. This is known as the DEP crossover frequency and can be defined as:

$$f_{cross} = \frac{1}{2\pi}\sqrt{\frac{(\sigma_m - \sigma_p)(\sigma_p + 2\sigma_m)}{(\varepsilon_p - \varepsilon_m)(\varepsilon_p + 2\varepsilon_m)}} \tag{3.28}$$

DEP crossover frequency can also be written in terms of the membrane conductance and capacitance per unit area[73]:

$$f_{cross} = \frac{\sqrt{2}}{8\pi R C_\mu}\sqrt{\left(4\sigma_m - R g_\mu\right)^2 - 9R^2 g_\mu^2} \tag{3.29}$$

The DEP induced particle velocity is directly proportional to the DEP force but also includes the viscous drag force imposed on the particle by the fluid[74]:

$$u = \frac{F_{DEP}}{6\pi R\eta} + \left(u_0 - \frac{F_{DEP}}{6\pi R\eta}\right)e^{-t/\tau} \tag{3.30}$$

Where u is the DEP-induced velocity of the particle, η is the viscosity of the suspending medium, and u_0 is the initial velocity. The time constant τ is given by[72]:

$$\tau = \frac{m}{6\pi R\eta} \tag{3.31}$$

where m is the mass of the particle. The momentum relaxation time, τ, in on the order of microseconds for a typical cell.

3.5 Electrorotation

The inclusion of losses in the effective dipole moment of the particle now allows for torque to be exerted on the particle until the induced dipole of the particle and the direction of the electric field are aligned. If however, the electric field is rotating, the particle will experience a continuous torque as the induced dipole tries to "catch up" to the electric field. If the field is rotating counter-clockwise it can be written in the vector phasor form:

$$\vec{E}(x,y) = E_0(\hat{x} - j\hat{y}) \tag{3.32}$$

Where $\hat{x}$ and $\hat{y}$ are orthogonal unit vectors. If a spherical particle is introduced at the origin (the center of the electrodes in this case) its induced dipole moment is:

$$\vec{p}_{eff} = 4\pi\varepsilon_m K(\omega) R^3 E_0(\hat{x} - j\hat{y}) \tag{3.19}$$

The time average torque on the particle is given by:

$$T_{ROT} = -4\pi\varepsilon_m R^3 Im[K(w)]|E_0|^2 \tag{3.33}$$

The frequency-dependence of torque depends upon the imaginary portion of the Clausius-Mossotti factor. Torque is measured indirectly through analysis of the rotation rate which is also dependant on the viscous drag on the particle[75]:

$$R_{ROT}(\omega) = -\frac{\varepsilon_m Im[K(w)]\left|\vec{E}\right|^2}{2\eta}K \tag{3.30}$$

Where η is the medium viscosity and K is a scaling factor.

Chapter 4. Demonstration of an Oscillator-Based Signal Generation System

Due to the low-cost of commercially available inverter circuits used for cold-cathode fluorescent backlights, an oscillator-based system was chosen in order to initially demonstrate the cDEP concept. An oscillator-based system was constructed that provided an electric field to a microfluidic device that successfully demonstrated dielectrophoretic effects on cells. The results were presented in the journal Biomedical Microdevices in 2009[12].

4.1 Royer-type Inverter Operation

A basic two-transistor Royer-type inverter circuit is shown in Figure 10. NPN transistors Q1 and Q2 are alternatively driven to saturation by the base drive provided by the feedback winding on transformer T1[76].

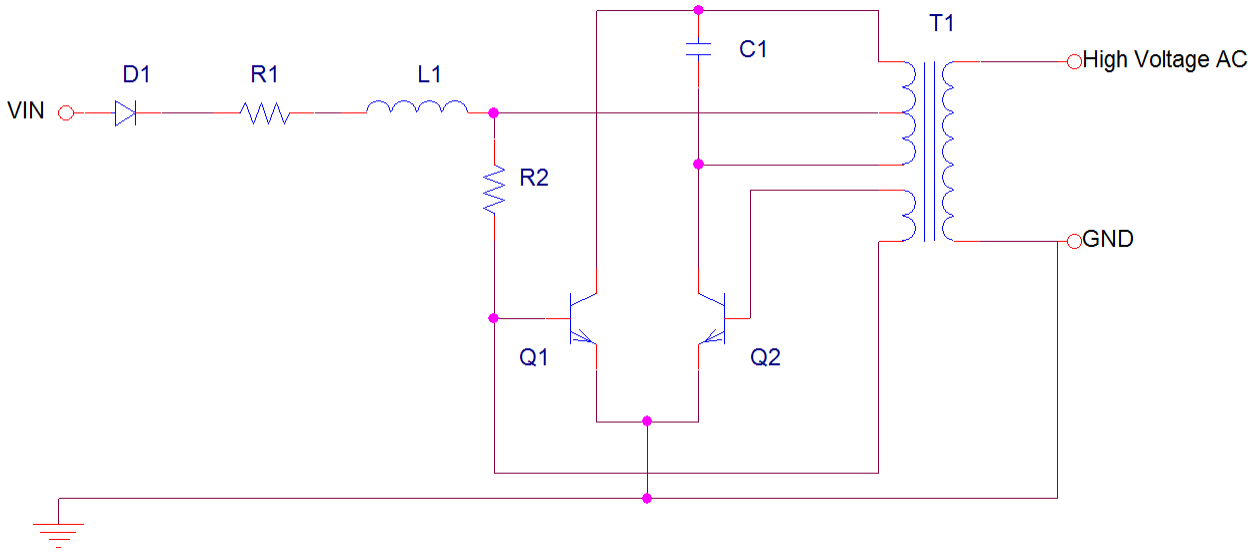

Figure 10: A two transistor inverter circuit intended for driving cold cathode fluorescent lamps.

The supply inductor L1 and primary capacitance C1 force the circuit to run sinusoidally thereby providing the preferred output voltage waveform to the microfluidic device. The operating frequency is determined by the primacy capacitance and the inductance of the transformer's primary winding which form a parallel resonant circuit:

$$f_O = \frac{1}{2\pi\sqrt{L_p C1}} \tag{4.1}$$

It is very important to note that the collector of each transistor is subjected to a voltage [76]:

$$V_C = 2 \times \frac{\pi}{2} \times V_{IN} = \pi V_{IN} \tag{4.2}$$

This is caused by the 2:1 autotransformer effect exhibited by each half of the transformer's center-tapped primary and the relationship of average to peak voltage of a sine wave. Because these circuits typically operate on low DC voltages, a very large transformer turns ratio is required to produce output voltages capable of igniting the lamp. This large turns ratio may have the detrimental effect of allowing the secondary load to become a dominant factor in the resonant frequency of the system. In the case of cDEP devices, the load they present to the oscillator tends to increase the resonant frequency of the system. Because the total impedance of a cDEP device

is a function of the device geometry, experimental fluids, and the system parasitics, the deviation from the no-load resonant frequency is fairly difficult to predict. In the case of the JKL Components inverter used in the system presented in this section, the frequency of oscillation increased by approximately 30 kHz with the connection to a microfluidic device.
One advantage of this system is that the circuits are capable of very high output voltages as is shown in Figure 11. The image from an oscilloscope shows a 2000 Volt peak-to-peak sine wave at 91 kHz produced by a 12 VDC CCFL inverter.

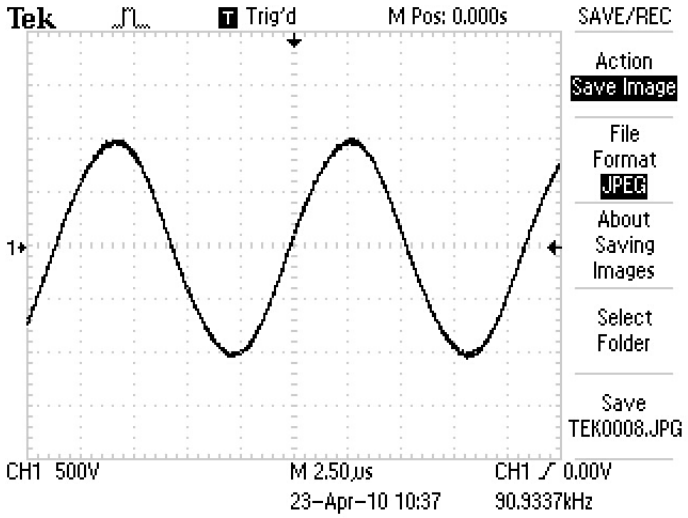

Figure 11: Oscilloscope waveform of the output of a CCFL inverter circuit. The voltage is approximately 2000V (peak to peak) at 91kHz.

Another advantage of this system is that the output voltage of the circuit is directly proportional to the input DC voltage and this relationship remains linear over a fairly large input voltage range. This concept was demonstrated for a 5Vdc inverter circuit and is shown in Figure 12.

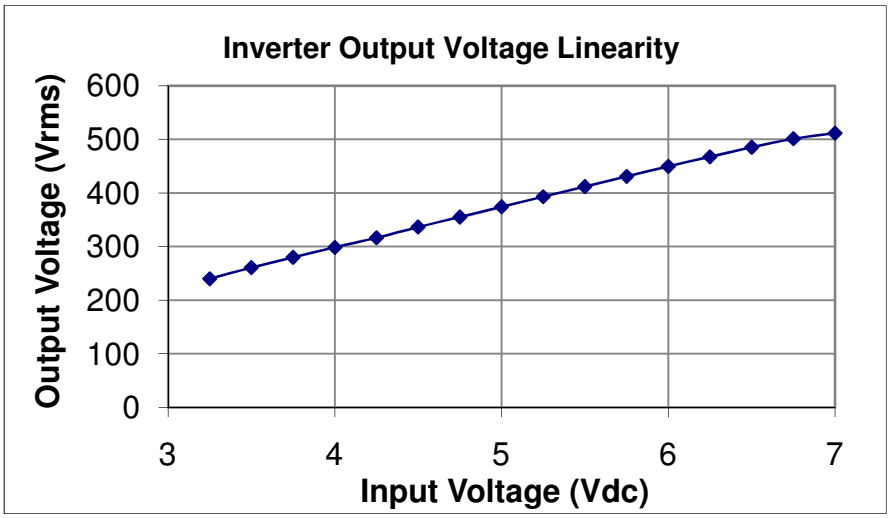

Figure 12: Plot showing the highly-linear nature of inverter circuit output voltage as a function of input DC voltage.

The obvious downside of this type of system is that the frequency of oscillation is fixed by the transformer inductance and capacitor C1 and cannot be varied. Therefore, oscillator based systems are difficult to "fine tune" in order to exploit the frequency dependence of DEP force.

The introduction of switched passive components would allow for the resonant frequency of the system to be varied.

4.2 Experimental Setup

Two commercially available inverter circuits (BXA-12576, JKL Components Corp., USA) were modified to provide a high-frequency and high-voltage AC signal for the device. These circuits exhibited resonant frequencies of 85 kHz and 125 kHz. A DC input voltage was provided by a programmable DC power supply (PSP-405, Instek America Corp., USA) which allowed adjustment of the output voltage amplitude by varying the DC input voltage. This technique allowed the output amplitude of the power supplies to be varied from approximately 100 Vrms to 500 Vrms. A three-resistor voltage divider network, with a total impedance of one megaohm, was added to the output of each inverter circuit in order to provide a scaled (100:1) output voltage to an oscilloscope (TDS-1002B, Tektronix, USA) which facilitated monitoring the frequency and magnitude of the signal applied to the microfluidic device. All circuitry was housed in a plastic enclosure with proper high-voltage warnings on its exterior and connections were made to the microfluidic device using high-voltage test leads. A photograph of the electronics is shown in Figure 13.

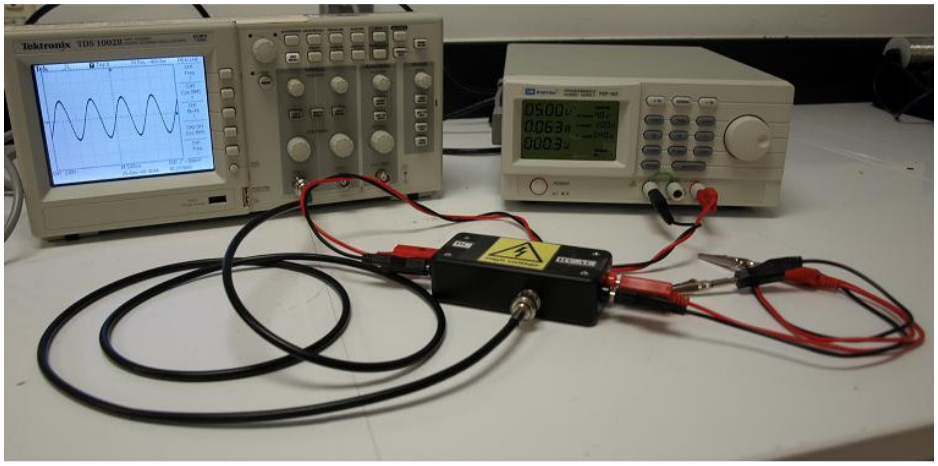

Figure 13: Photograph of an enclosed inverter circuit for cDEP experimentation. The circuit is powered by a standard DC power supply and its output voltage and frequency are monitored through a 100:1 voltage divider on and oscilloscope.

Pipette tips, inserted in the punched holes in the PDMS portion of the device, were used as reservoirs for fluidic connections to the channels. Pressure driven flow (10 to 15µl/hr) was provided by an imbalance in the amount of the sample in these reservoirs of the main channel. An inverted light microscope (Leica DMI 6000B, Leica Micro-systems, Bannockburn, IL) equipped with a digital camera (Hamamatsu EM-CCD C9100, Hamamatsu Photonics K.K. Shizuoka Pref., 430-8587, Japan) was used to monitor cells in the main channel. Microfluidic devices were placed in a vacuum jar for at least half an hour before running the experiments to reduce priming issues and then the side and main microchannels were filled with PBS and DEP buffer, respectively.

The THP-1 human Leukemia monocytes, MCF-7 breast cancer cells, and MCF-10A breast cells were washed twice and resuspended in our prepared DEP buffer (8.5% sucrose [wt/vol], 0.3% glucose [wt/vol], and 0.725% [vol/vol] RPMI) (Flanagan et al. 2008). The electrical conductivity of the buffer was measured with a Mettler Toledo SevenGo Pro conductivity meter (Mettler-

Toledo, Inc., Columbus, OH) to ensure that its conductivity was 100μS/cm. These cells were observed to be spherical when in suspension. The measured diameters of the cells with the corresponding standard deviations (n=30) are given in Table 2.
The average velocity of the THP-1, MCF-7 and MCF-10A cells in our microfluidic device was measured along the centerline a-b in Figure 15 from point 1 to point 4. Time-lapse videos were recorded of the cells motion before and after applying an AC electric field through the platinum electrodes inserted in the side channels. These recorded videos then were converted to JPEG files using the Leica software, (Leica DMI 6000B, LAS AF 1.6.3 Leica Micro-systems, Bannockburn, IL), in order to measure the traveling time of the target cells for a known specific distance in the main channel. These measurements were performed before and after inducing the electric field in the main microfluidic channel.

4.3 Numerical Modeling

The microfluidic device was modeled numerically in Comsol multi-physics 3.4 using the AC/DC module (Comsol Inc., Burlington, MA, USA). Because DEP depends on the gradient of the electric field the first step in modeling was to determine the electric field distribution within a channel's geometry. This was done by solving for the potential distribution, φ, using the Laplace equation, $\nabla^2 \varphi = 0$. The boundary conditions used are prescribed uniform potentials at the inlet or outlet of the side channels.

Table 2: Electrical properties of the materials and fluids used [12].

Electrical Properties Materials	Electrical Conductivity (S/m)	Relative Electrical Permittivity
PDMS	0.83 e-12	2.65
PBS	1.4	80
DEP Buffer	0.01	80

The values for the electrical conductivity and permittivity of the PDMS, PBS, and DEP buffer that were used in this numerical modeling are given in Table 2. PBS and DEP buffer electrical properties are used for the side and main microfluidic channels, respectively. Figure 14 shows the areas with an electric field intensity above, 0.1, 0.15, and 0.2 kV/cm. Figure 15 shows the distribution of the gradient of the electric field with in the device. The areas of non-uniformity in the electric field are directly associated with variations in the thickness and geometry of the PDMS separating the electrode reservoirs from the sample channel.

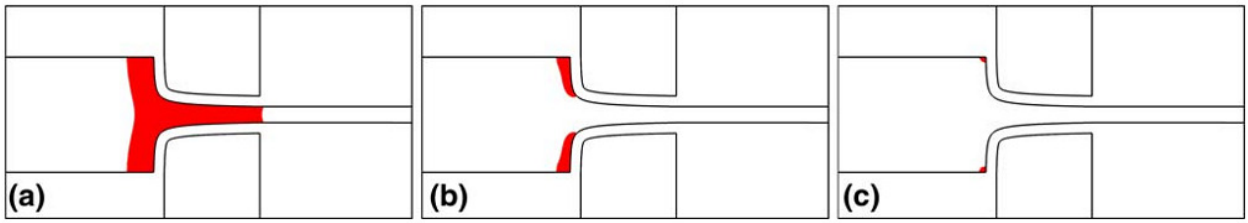

Figure 14: Electric field surface plot for an applied signal of 250Vrms at 85 kHz. Areas indicated in red have an electric field intensity more than (a) 0.1 kV/cm, (b) 0.15 kV/cm, (c) 0.2 kV/cm.

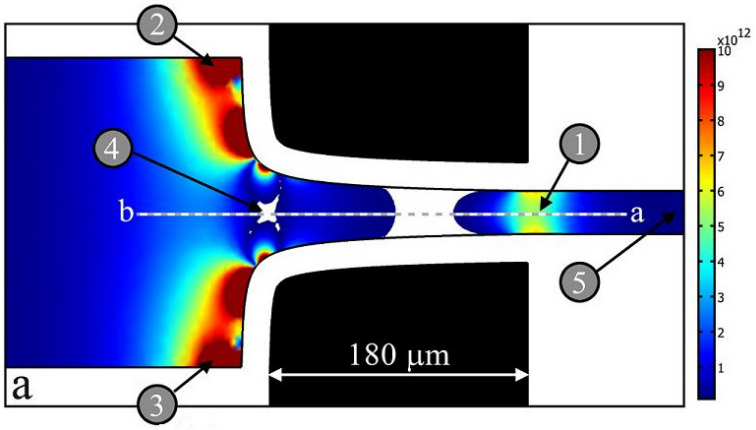

Figure 15: Surface plot of the gradient of the electric field in the device for an 250Vrms, 85kHz signal. Units are $kg^2mC^{-2}S^{-4}$

This numerical modeling accurately predicted the regions in the device most likely to exhibit high DEP forces on the target cells given the limitations of the signal generation equipment.

4.4 Results

Figure 16 shows the experimental results we attained using MCF-7 breast cancer cells and THP-1 leukemia cells in our device. The images are comprised of multiple images superimposed to show the progression of a single cell through the device without an applied field (a) and with an applied field (b). The behavior of cells traveling through the device under static conditions was observed to be significantly different than when an electric field was applied to the device.

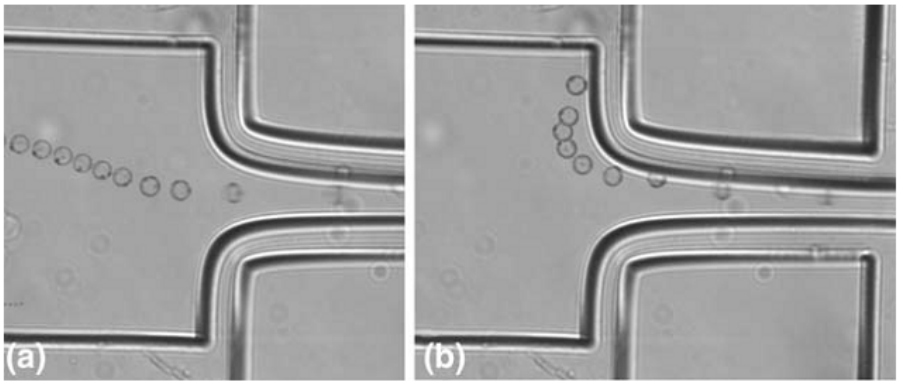

Figure 16: Multiple superimposed images showing the tragectory of a single cell through the cDEP device. (a) the cell is moving from right to left without an applied field (b) A 250 Vrms 85 kHz is applied to the channel causing a positive DEP response in the cell.

Three induced DEP responses were studied: rotation, velocity changes, and chaining. Under a pressure driven flow, without an applied electric field, it was observed that THP-1 leukemia and MCF-7 breast cancer cells flow through the main microfluidic channel from right to left without any disruption or trapping. The cells were observed to be trapped, experiencing a positive DEP force, once an AC electric field at 85 kHz and 250 Vrms was applied. Their velocity decreased at the intersection between the main and the side channels where the thin PDMS barriers are located. With the same electrical boundary conditions we did not observe any trapping or cell movement disruption for MCF-10A normal breast cells. These results indicate that the cells exhibited positive DEP at 85 kHz in our device. The cells were observed to move faster along the centerline of the sample channel in Figure 15 from point 5 to point 1 when the electric field was

applied as compared to their velocity due to pressure driven flow. As shown in Figure 15, the magnitude of the DEP force is high at point 1. Because the DEP force is positive at 85 kHz, the cells are attracted to this point. Therefore, as the cells approach point 1 from the right, the positive DEP force is in the direction of the pressure driven flow, causing the cells to move faster down the channel. Conversely, the average velocity of the cells in the area between the thin PDMS barriers (from 1 to 4) decreases when the voltage is applied because the positive DEP force now acts in the opposite direction of the pressure driven flow.

Table 3: Experimental results of three different cell types used to demostrate DEP.

Cell Velocity Cell line	Diameter (μm)	Uon (μm/s)	Uoff (μm/s)	Uoff- Uon(μm/s)	Uon/Uoff	Ω (rad/s)
THP-1	15.4 ±2	240±13	392±21	152±19	0.61±0.08	8.1±0.66
MCF-7	18.5±2.5	387±7	476±17	89±17	0.81±0.04	19.4±2.9
MCF-10A	18.2±2.1	310±17	313±16	3±24	0.99±0.076	N.A.

Table 3 compares the average induced velocities of the cells with respect to their average velocities under pressure driven flow. The results show that there is a statistically significant difference in the cells velocities when the field is applied. The same experiments with the same buffers and electrical boundary conditions were performed on MCF-10A breast cells without noticeable trapping or disruption, which shows that the electrical properties of the normal breast cells are different compared to the MCF-7 breast cancer cells. There was a great tendency for cells to move towards the corners in the main channel. This agrees with our numerical results, which show there is a high gradient of the induced electric field at the corners, which causes a strong positive DEP force and pulls cells towards these zones of the main microfluidic channel. Figure 17 displays the chaining effect cells that are polarized in an electric field have on other fields. The dipole induced in the cell by the electric field exerts a force on the cells around it, causing the cells to chain pole-to-pole parallel to the direction of the electric field. The chains in the image are also effected by fluid flow in the channel.

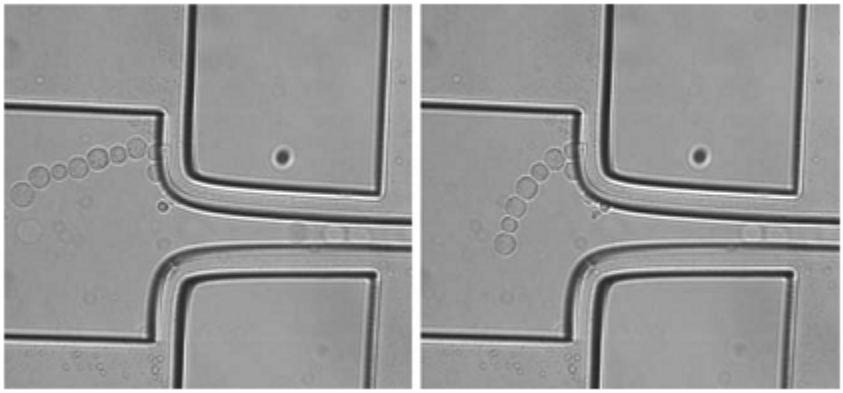

Figure 17: The "pearl chain" DEP response resulting from the cell's local distortion of the electric field.

Chapter 5. Demonstration of an Amplifier-Based Signal Generation System

While the oscillator-based system of the previous chapter was able to successfully demonstrate that the concept of cDEP was valid, it revealed the need for reliable control of both the voltage and the frequency of the applied signal in order to maximize the DEP force on the target cell. To that end, a signal generation system more suitable to the laboratory research environment was developed consisting of a wideband power amplifier and a high voltage transformer. The added flexibility this system provides has allowed cDEP to demonstrate both positive and negative DEP in target particles[14] and the selective isolation of live cells from dead ones[13].

5.1 System Description

The basic system configuration is shown in Figure 18. The initial signal is produced by a standard laboratory function generator and preliminary amplification is performed by a power amplifier. The output of the power amplifier is connected to a custom-wound high-voltage transformer in order to step-up the voltage to the levels required by cDEP microfluidic devices.

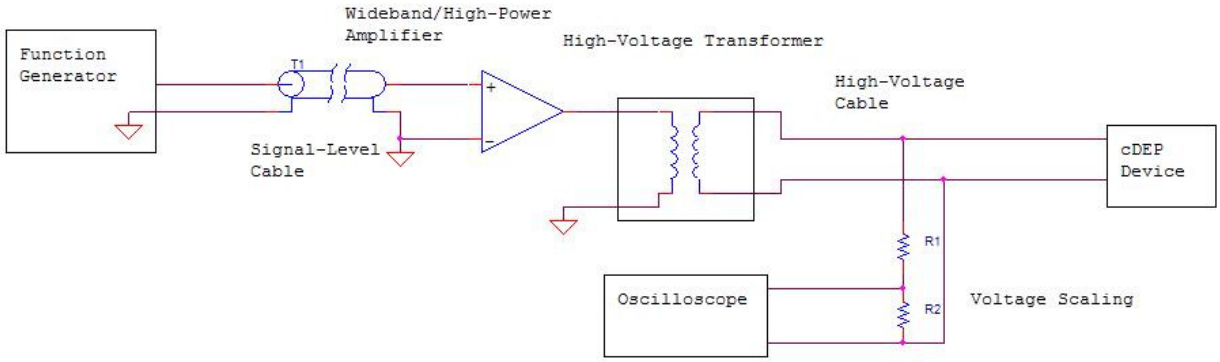

Figure 18: System diagram of an amplifier-based solution for signal generation for cDEP devices.

The system was developed with direct cooperation from Amp-Line Corp., a company specializing in wideband power amplification for applications in the industry, military, and research organizations. Waveform generation was performed by a function generator (GFG-3015, GW Instek, Taipei, Taiwan) whose output was then fed to the wideband power amplifier (AL-50HF-A/VT, Amp-Line Corp., Oakland Gardens, NY). This amplifier is a modified version of Amp-Line's AL-50HF-A power amplifier and the specifications are given in Table 4.

Table 4: Amp-Line power amplifier specifications.

Frequency Range	30Hz-1MHz
Input Voltage	0-2Vrms
Output Voltage	0-22.5Vrms
Output Power	50W

The wideband power amplifier performed the initial voltage amplification of the signal and provided the necessary output current to drive a custom-wound high-voltage transformer. The transformer consists of a 212 turn secondary wound in five sections of 4 layers each, coupled to a 5 turn primary through a ferrite ring core (TX74/39/13, Philips Components, San Jose, CA). Further transformer specifications are displayed in Table 5. The transformer is enclosed in a

grounded metal chassis featuring high-voltage connections. Frequency and voltage measurements were accomplished using an oscilloscope (TDS-1002B, Tektronics Inc. Beaverton, OR) connected to a 100:1 voltage divider at the output of the transformer.

Table 5: Amp-Line wideband transformer specifications.

Primary Voltage Rating	21 Vrms
Secondary Voltage Rating	1000 Vrms
Turns Ratio	42 to 1
Leakage Inductance	1 uH (pri)

The transformer was placed inside a grounded cage with the microscope and attached to the devices using high-voltage wiring. The amplifier based system is displayed in Figure 19.

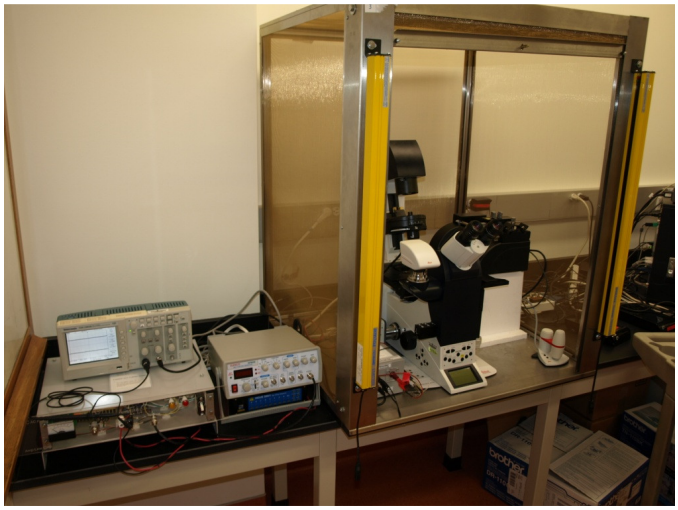

Figure 19: Wideband, high-frequency signal generation equipment used for cDEP experimentation.

This system is ideally suited to the laboratory environment. By relying upon a function generator to create a sine wave, the system allows for the modification of both voltage and frequency of the applied signal in order to optimize the DEP force on the target particle. Also, by incorporating computer control of the function generator, this system may be used as part of an automated sample enrichment platform.

The use of an amplifier and transformer combination was selected because it allows for the generation of signals of much higher voltages than an amplifier alone. However, the ability to generate signals of high-amplitude comes at the cost of output linearity. The voltage step-up (gain) achieved by the transformer is shown in Figure 20. As can be seen in the plot the system is fairly linear below 100 kHz. As frequency is increased the voltage gain is decreased until a resonance in the system is reached at approximately 800 kHz. Beyond this resonance point, the ability of the transformer to increase the signal's voltage diminishes rapidly. To date cDEP experimentation has relied upon signals with frequencies far below the resonance point of the transformer. Also, the use of a separate amplifier and transformer allows for the transformer to be replaced with units capable of performing voltage step-up in other bandwidths. If the high-voltage provided by the transformer is not necessary, it would be preferable to remove the

transformer from the system in order to preserve a linear response across a much larger frequency range.

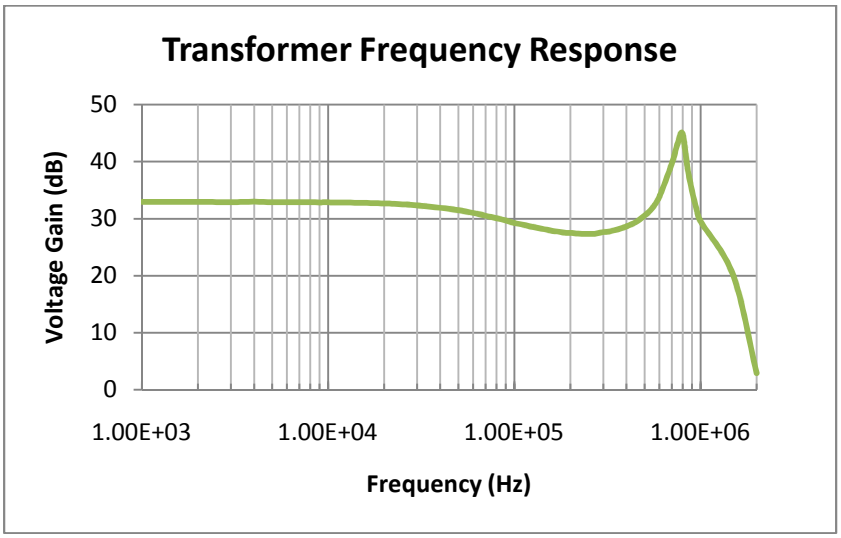

Figure 20: Amplitude plot of the frequency-dependant voltage gain of the transformer.

5.2 Diverse Particle Enrichment Demonstration

The capabilities this system provides have allowed the BEMS laboratory at Virginia Tech to demonstrate a much broader range of DEP effects on a more diverse selection of target particles. This concept was demonstrated in an invited paper to the Journal of the Association of Laboratory Automation[14]. The electronics presented above, combined with a cDEP device were able to demonstrate the enrichment of THP-1 human leukemia cells from a sample also containing 10 μm diameter polystyrene microspheres through positive DEP force. The system also showed the concentration of 2 μm polystyrene microspheres in a sample of dionized water through negative DEP force.

Live samples of THP-1 human leukemia monocytes were prepared in the same manner as was described in the previous chapter. Carboxylate-modified polystyrene microspheres (Molecular Probes, Eugene, OR) having a density of 1.05 mg/mm^3 and diameters of 2 and 10 μm were used at a dilution of 1000 from a 2% by weight stock suspension. Bead suspensions were sonicated between steps of serial dilution and before use. The background solution was deionized water with a conductivity of 86 ms/cm. Live THP-1 cells were stained using cell trace calcein red-orange dye (Invitrogen, Eugene, OR). The stained cell sample and the 10-μm beads sample were mixed in a ratio of 1:1.

Numerical modeling was again used to determine relevant experimental conditions, such as applied voltage and frequency. Experimental values for the voltage and frequency must be chosen to provide sufficient DEP force on the target particles without exceeding the dielectric breakdown voltage of the PDMS barriers (280 V for a 20-μm barrier). Because of the capacitive properties of the thin PDMS barrier between the side channels and the main channel, the induced electric field inside the main channel is strongly dependent on the frequency and the applied voltage. Hence, a minimum frequency is required to provide a strong gradient of the electric field with respect to a specific voltage for microparticle manipulation. A 70-Vrms sinusoid at 300 kHz was found to provide significant DEP force in the microfluidic channel without damaging the

device. The electric field intensity surface plot in the main channel of the device at the experimental parameters is shown in Figure 21(A).

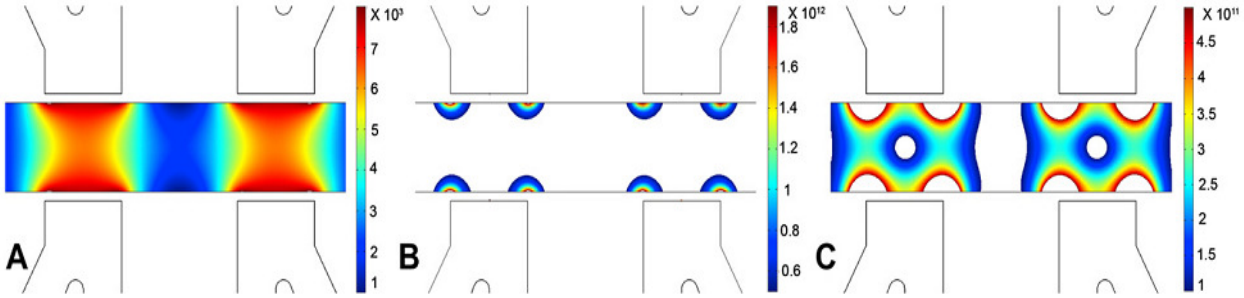

Figure 21: Results of COMSOL numerical modeling of a cDEP device. (A) Electric field intensity in V/m (B and C) The gradient of the electric field with two representative ranges[14].

It is important to note that the electric field intensity does not reach 0.1 kV/cm, which is not strong enough to kill cells. The trapping regions and the cell's trajectory through the microfluidic device can be predicted using the numerical modeling, as DEP cell manipulation is strongly dependent on the gradient of the electric field. The highest gradient of the electric field is estimated to appear at the edges of the side channels, as shown by the numerical results found in Figure 21B. However, there is still a sufficient gradient of the electric field at the middle of the channel to manipulate the microparticles as shown in Figure 21©.

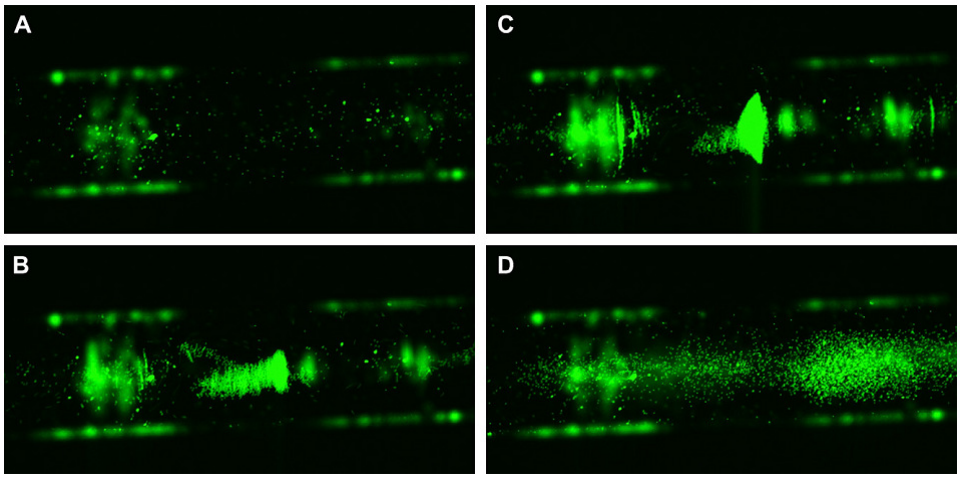

Figure 22: 2 um polystyrene microbeads suspended in dionized water and concentrated through negative DEP. (A) No external field applied. (B) 30 seconds after the application of a 190 Vrms 300 kHz signal (C) 50 seconds after applying the signal (D) The signal is removed and trapped beads are released[14].

Particle concentration through negative DEP was displayed using 2-μm beads suspended in deionized water at 190 Vrms at 300 kHz. These experimental results are shown in Figure 22. As is consistent with a negative DEP response, the beads are grouped in regions away from high gradients of the electric fields, which, in this case, is in the centerline of the channel. The inability to focus the microscope on all of the trapped beads simultaneously indicates that the beads were trapped at multiple heights in the main channel.

The selectivity of the device to differentiate two different particles with almost the same size was examined through separation of THP-1 cells from 10 μm beads. The THP-1 cells were observed

to be trapped at 70 Vrms and 300 kHz, and the 10 μm beads went through the main channel without significant DEP disturbance Figure 23.

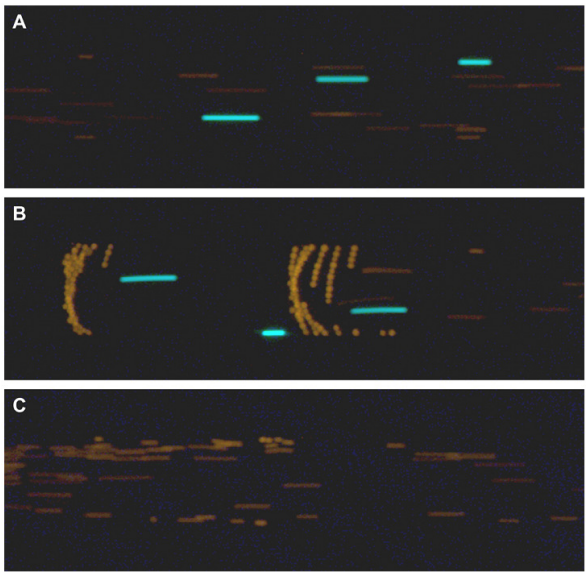

Figure 23: Selective trapping of live THP-1 cells (orange) from a mixture also containing 10 um polystyrene microspheres (blue). (A) Cell motion without an applied field due to pressure-driven flow (B) THP-1 cells are trapped by using a 70 Vrms 300 kHz signal (C) The field is removed to release the cells[14].

5.3 Selective Trapping of Live Cells from Dead

In this study, the ability of cDEP to selectively isolate and enrich a cell population was investigated. This was demonstrated through the separation of viable cells from a heterogeneous population also containing dead cells. Viable THP-1 Human leukemia cells were successfully isolated from dead (heat treated) cells without lysing. The separation of viable and non-viable cells is a critical starting point for this new technology to move towards more advanced applications. By using viable/non-viable separation as a model for new cDEP applications, a new generation of cDEP devices can be tailored around these results which were reported in Lab on a Chip in February of 2010[13].

Live samples of THP-1 human leukemia monocytes were washed twice and re-suspended in a buffer used for DEP experiments (8.5% sucrose [wt/vol], 0.3% glucose [wt/vol], and 0.725% RPMI [wt/vol]) to 10^6 cells/mL. The cell samples to be killed were first pipetted into a conical tube and heated in a 60^{o}C water bath for 12 min; an adequate time determined to kill the majority of the cells in the sample. To enable simultaneous observation under a fluorescent microscope, cells were stained using a LIVE/DEAD Viability/Cytotoxicity Kit for mammalian cells (Molecular Probes Inc.). Calcein AM, which is enzymatically converted to green fluorescent calcein, was added to the live cell sample at 2 mL per mL of cell suspension. Ethidium homodimer-1 (EthD-1) was added to the dead cell sample at 6 mL per mL of cell suspension. This can only pass through damaged cell membranes and upon nucleic acid-binding produces a red fluorescence. The two samples were then vortexed for 5 min, washed once and re-suspended in DEP buffer. The live and dead suspensions were then mixed together in one conical tube with a final concentration of 10^6 cells mL and final conductivity of 110–115 mS/cm measured with a SevenGo Pro conductivity meter (Mettler-Toledo, Inc., Columbus, OH). Live and dead cells were indistinguishable under bright field evaluation.

Two cDEP devices were fabricated for this study using the technique given previously in this document and are shown in Figure 24. Again, COMSOL numerical modeling was used to determine experimental conditions that were likely to cause trapping of live cells in the sample channel.

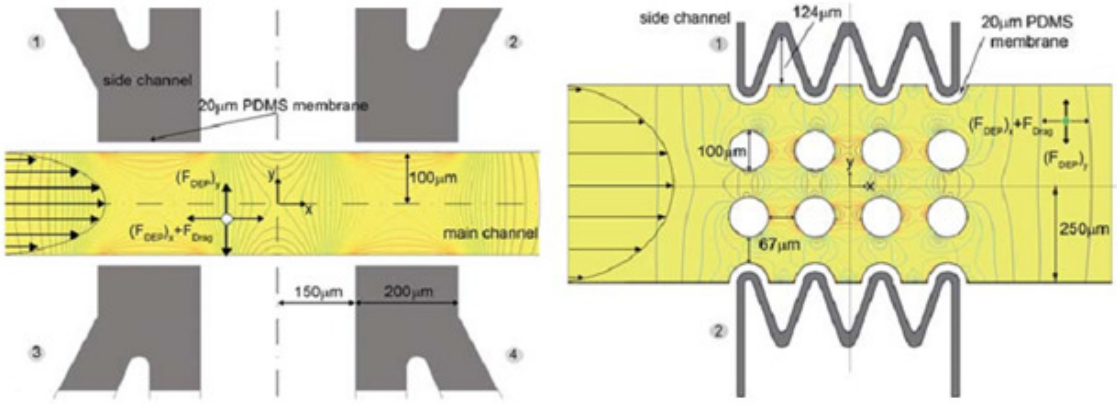

Figure 24: Two cDEP microfluidic devices used to demonstrate DEP separation of live cells from dead. (Left) Device 1: The prototype cDEP device used to demonstrate the rapid fabrication technique and the validity of numerical modeling (Right) Device 2: A second generation cDEP device featuring pillars in the sample channel to create regions of DEP away from the side electrode reservoirs[13].

Device 1 was used to verify the numerical modeling techniques used to determine experimental conditions. This was accomplished by determining at what frequency at least 80% of live cells were trapped for a given voltage. Experiments were conducted at 50 Vrms,75Vrms, 100 Vrms, 125 Vrms and 150 Vrms. Trapping boundary conditions for this device were determined through visual inspection of the cells passing through the main channel. The electric field was maintained for 30 s during each experiment. Eight trials were conducted at each voltage and the corresponding frequencies were recorded where 80% trapping was observed. These results are presented in Figure 25.

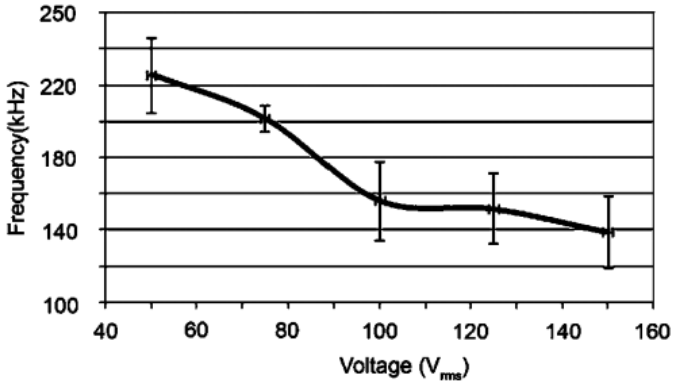

Figure 25: Frequency required to trap 80% of the cells flowing through the devices for a given voltage[13].

The insight provided by device 1 allowed for the necessary gradient of the electric field for trapping to be determined and this information was used to determine experimental conditions for the second device. The trapping efficiency for this device was determined for voltages of 20 Vrms, 30Vrms, 40Vrms, 50Vrms and frequencies of 200 kHz, 300 kHz, 400 kHz, 500 kHz at a constant flow rate of 0.02 mL/h. Experimental parameters were tested at random to mitigate any variation in cell concentration, flow rate, device functionality and other experimental variables.

Additionally, trapping efficiency was calculated at 0.02 mL/h,0.04 mL/h, 0.06 mL/h, and 0.08 mL/h, with electrical parameters held constant at 500 kHz and 30 Vrms.

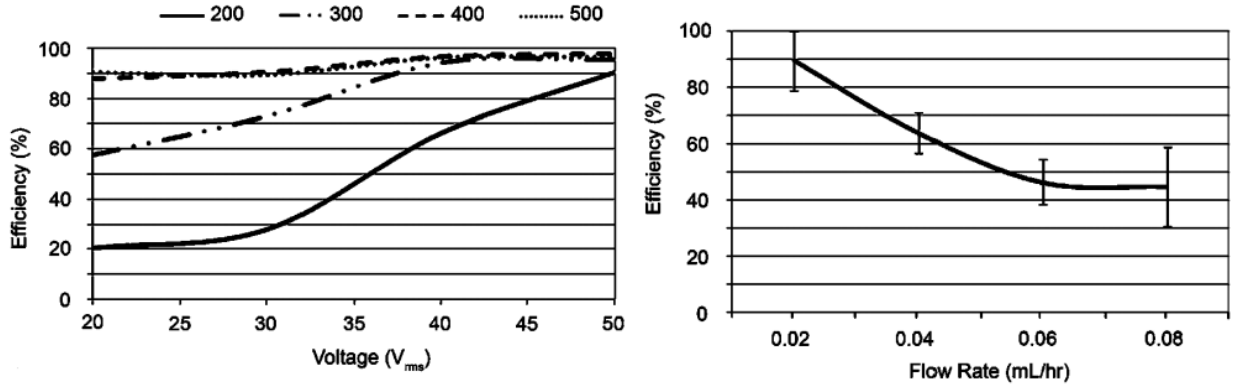

Figure 26: (Left) Trapping efficiency versus applied voltage for four different frequencies in device 2. (Right) Trapping efficiency of device 2 as flow rate was increased through the sample channel[13].

Electrical parameters were selected randomly for each experiment for a total of five trials at each combination. The electric field was maintained for 30 s during each experiment. During the 30 s interval, all cells entering the trapping region of the device (the region containing pillars in the main channel) were counted, representing the total number of cells.

Both devices successfully exhibited the trapping of live cells, while dead cells pass through unaffected. This is illustrated in Figure 27.

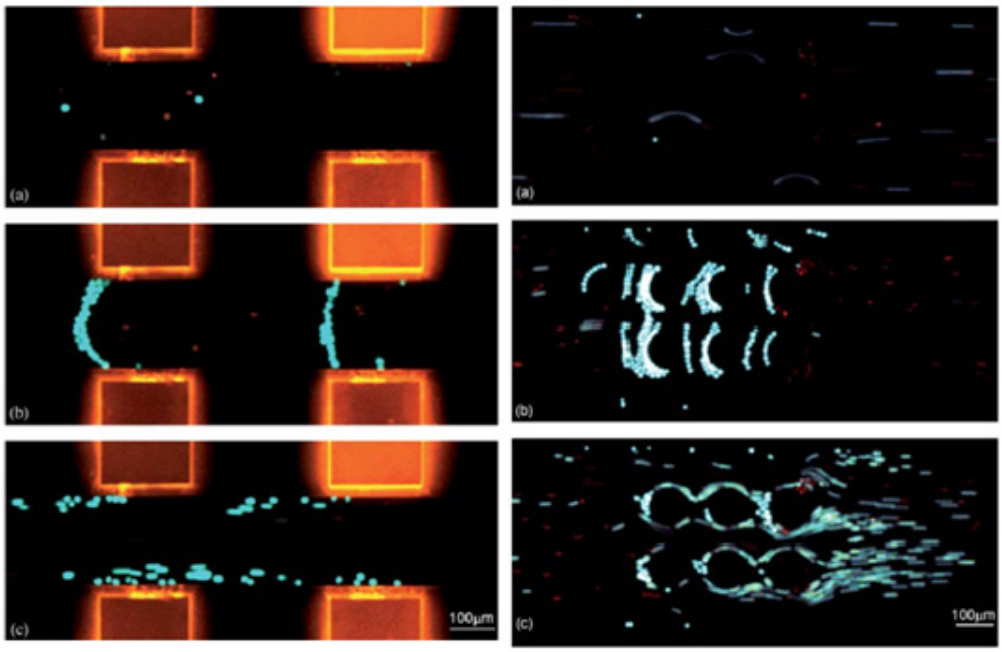

Figure 27: (Left) Experimental results for device 1. (a) Cells move through the device from right to left without an applied field. (b) Live THP-1 cells (blue) are trapped in region of high DEP 30 s after applying a field. (c) The field is removed and the trapped cells are released. (Right) This same process is applied to device 2[13].

The amplifier and transformer based system presented in this section allowed for a very broad range of experimental variables to be tested in both devices; allowing for the DEP response in to be maximized.

Chapter 6. Electronics for Rotational Spectroscopy

One of the challenges in performing ROT spectra experiments is the difficulty of generating four sine waves with a 90 degree phase shift over a wide range of frequencies. This is not a trivial problem when one considers the range of frequencies over which ROT spectra measurements are to be made. The original solution to this problem was through the use of passive components to provide the phase shift. However, generators using these networks were limited to a single frequency such that their components had to be switched to provide an accurate phase shift at a new frequency[61]. Arnold and Zimmerman were the first to provide a solution to this problem using electronic circuitry. Their device utilized the phase shifted current through a capacitor to provide the 90 phase difference. A feedback look enclosing the circuitry allowed the system to provide a flat amplitude response over a 20:1 frequency range. Through the use of 5 separate networks the group was eventually able to construct a circuit that operated from 50 Hz to 5 MHz[61]. Modern groups have begun to rely upon specialized function generation equipment to produce the necessary signals[41, 70]. While this solution provides very high quality output signals it is often prohibitively expensive. This section describes an alternative method to generate the necessary phase-shifted sine waves for electrorotation using a commercially available direct digital synthesis (DDS) integrated circuit. The quality of modern DDS circuits and operational amplifiers allows the system described here to produce four sine waves of useable voltages over a bandwidth of 10 Hz to 100 MHz. Through the use of commercially available demonstration modules this system was rapidly prototyped for less than $1000.

6.1 System Description

The basic system configuration is shown in Figure 28. The basis for the electronics is a DDS IC normally used for in-phase/quadrature (I/Q) modulation in communication systems. These circuits are uniquely suited this task because they generate two sine waves with a 90 degree phase shift by design. Furthermore, their use in communication systems requires both wide bandwidth and a high quality output signal.

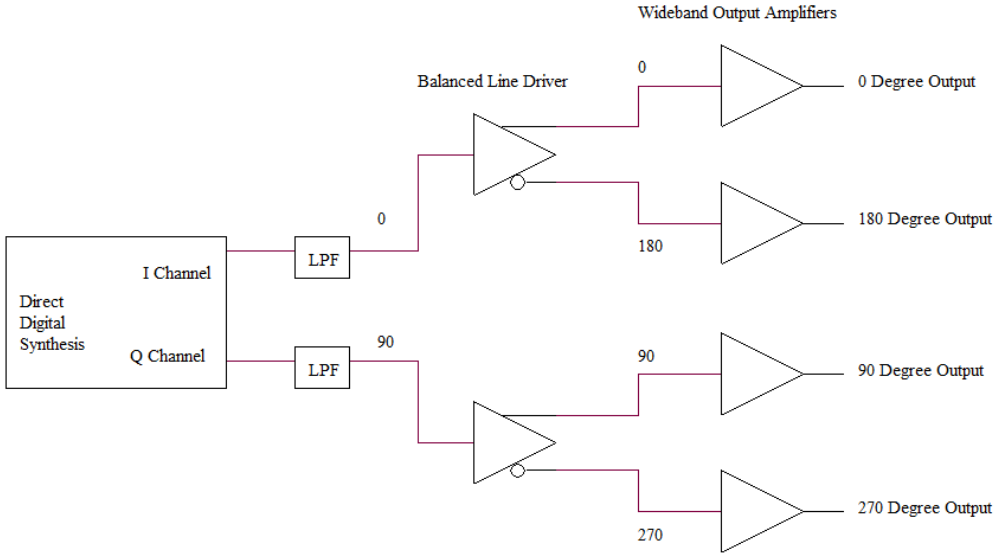

Figure 28: Block diagram of the system used to produce four sine waves with a 90 degree phase shift between the outputs.

The output from the I/Q synthesis chip is then filtered to remove clock noise inherent to the circuit and passed to a balance line driver. Balanced line drivers convert a single-ended signal into two symmetrical waveforms with a 180 degree phase shift. Therefore this stage of the system converts the original 0 and 90 degree signals into the necessary 0, 90, 180, and 270 degree shifted signals. It was also convenient to use this portion of the system to provide a preliminary voltage gain. The four signals are then further amplified to voltages capable of producing a measurable rotation in the cells before being sent over transmission lines to the probe array. Each section of the system is explained in further detail in the following sections.

6.2 Signal Generation

A highly stable quadrature DDS device from Analog Devices (AD9854, Analog Devices, Norwood MA) forms the backbone of the signal generation system. This device is capable of up to a 300 MHz clock rate allowing quadrature output signals of up to 150 MHz. These dual outputs can be tuned at a rate of up to 100 million new frequencies per second with an accuracy of 1 μHz (with a 300 MHz clock).

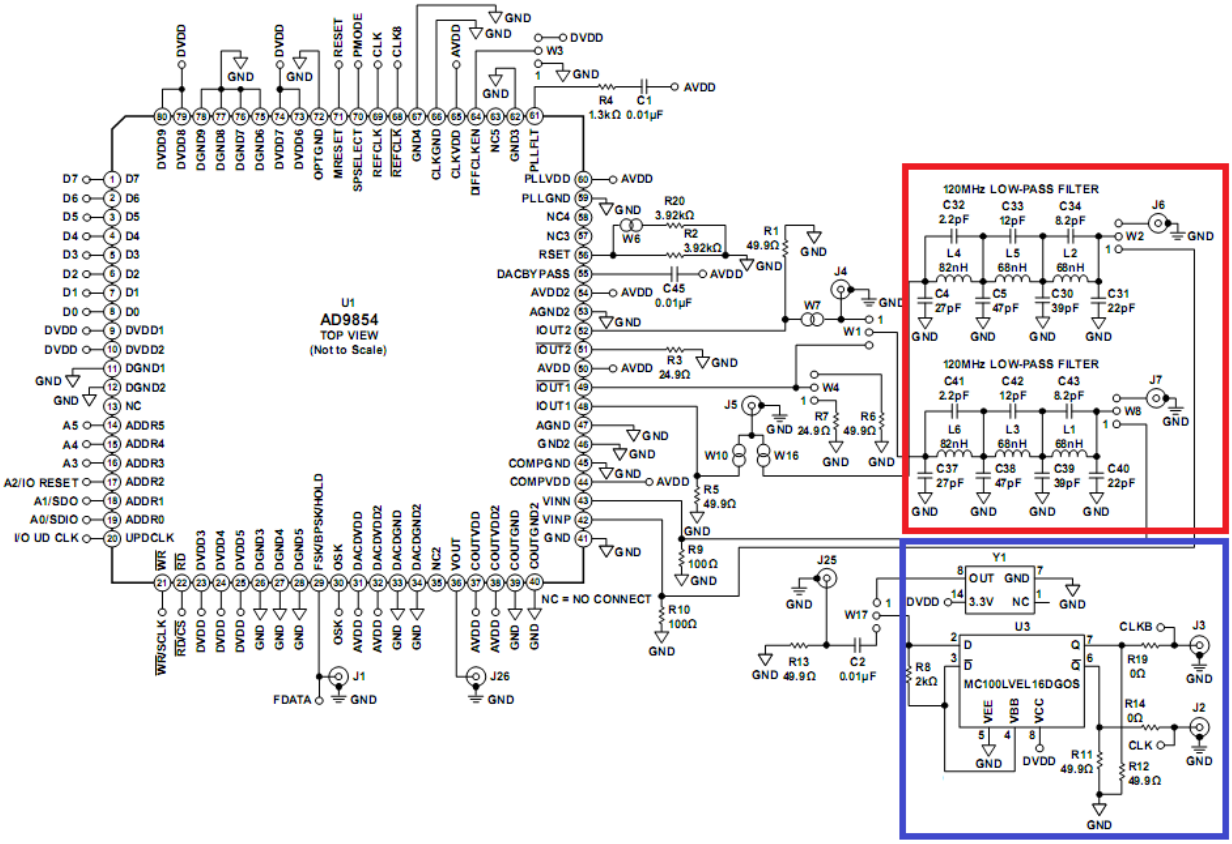

Figure 29: Schematic of the AD9854 DDS system as well as the clock generation circuitry(outlined in blue) and low-pass output filters(outlined in red). AD9854 datasheet, Analog Devices.

In order to speed the development of this system, the evaluation module for the AD9854 was chosen rather than the creation of an application specific printed circuited board. This decision was made for many reasons. To start, the evaluation module already included on-board circuitry for a computer interface, clock generation (except crystal) and low-pass filters on the outputs of both channels (Figure 29). Furthermore, the evaluation module features included software to control the frequency of the output signals and the more advanced features of the system (clock

multiplier, output amplitude, inverse sinc filtering). The incorporation of these features, with the fact that all high frequency PCB layout considerations had already been addressed, makes the evaluation module an invaluable asset to the rapid construction of this system. The only modifications necessary to the board were to install a 50 MHz crystal in the provided location and to switch the output connectors from SMB to SMA type.

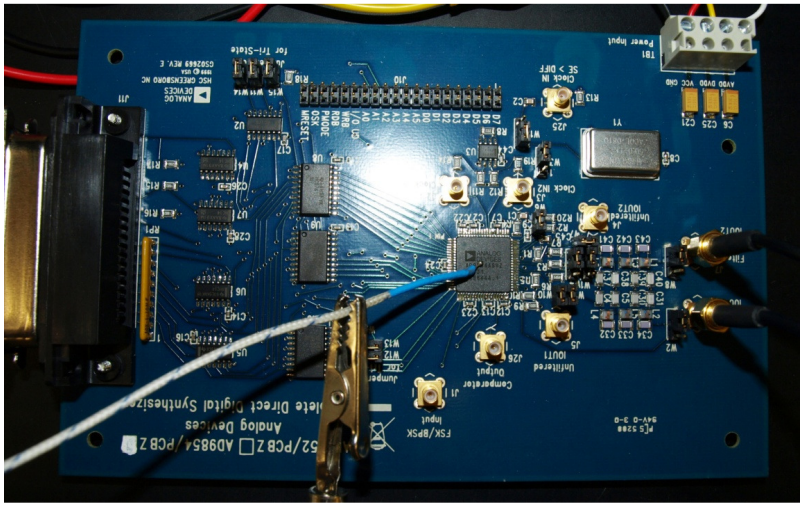

Figure 30: AD9854 evaluation module from Analog Devices. A thermocouple was attached to the DDS IC during configuration to ensure the system stayed within its usable temperature limits.

Interface with a computer system is made through the evaluation module's on-board parallel connector. Using the provided software from Analog Devices, the board was configured for an internal clock rate of 250 MHz as a compromise between thermal concerns and output signal quality. It was also found during configuration that by disabling the onboard inverse sinc filter, which is included to further linearize frequency response, the system could be run at a much lower temperature with minimal compromise in linearity. This was determined by monitoring the output signal of the board using a lock-in amplifier (SR-844, Stanford Research, Palo Alto, CA) while the temperature was measured using a thermocouple. This testing also showed that the nominal output of the evaluation module was 160 mVrms.

6.3 Balance Line Drivers and Initial Amplification

One half of the balanced line driver stage is shown in Figure 31. The circuit is comprised of an input impedance matching and DC blocking network, a Maxim MAX4449 differential line driver, and 50 ohm output impedance matching resistors. The Maxim MAX4449 differential line driver was chosen for its very high slew rate (6500 V/µS), wide small signal bandwidth (400 MHz), and high gain abilities. BNC connectors are used on the output of the circuit because the prototype system was designed to be modular and therefore connection to the next stage was to be made through a transmission line.

While connections to this stage are made with 50 ohm characteristic impedance transmission lines, the 50 ohm input impedance resistor was not chosen to minimize load reflections at high frequencies. Rather, the output filters on the AD9854 evaluation module are designed to be used with a 50 ohm load impedance and any variation from this load impedance causes non-ideal suppression of the clock noise from the board. The output of the DDS IC also has a DC offset imposed on the signal of approximately 100 mV. If this DC offset was not blocked, it would be

amplified by the subsequent stages, causing a large DC value to appear at the ouput of the system and most likely saturating the output amplifiers.

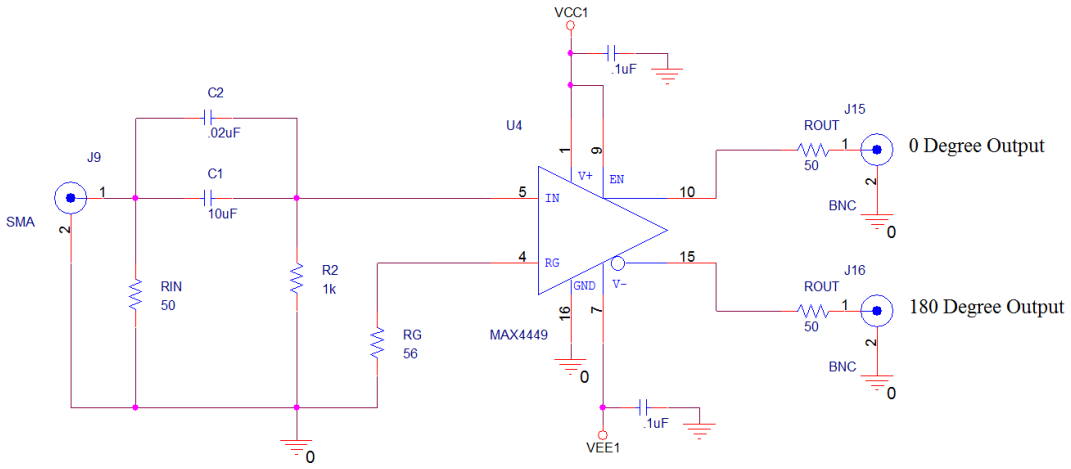

Figure 31: Schematic of one-half of the balanced line driver circuitry that provided phase-splitting and initial amplification.

In order to prevent this a DC blocking capacitance composed of C_1 and C_2 in parallel was added to the input with resistor R_2 to form an input pi network. The DC blocking capacitance was formed by paralleling a large value monolithic ceramic capacitor (C_1) with a high-frequency polystyrene capacitor (C_2). This was done to ensure that the impedance of the combination was free from non-linearities do to the equivalent series resistances and inductances of the individual capacitor's dielectrics. The corner frequency of the input network can be found using the equation:

$$f_{-3dB} \approx \frac{2.413}{2\pi C_{IN} R_2} = \frac{2.413}{2\pi(10.02\mu F)(1000\Omega)} = 38.32Hz \tag{6.1}$$

Where $C_{IN} = C_1 \parallel C_2$. The requirement for output down to very low frequencies would dictate the use of a very large input capacitance and a very large value for R_2. However there are more factors in determining appropriate values for these components. To start, the MAX4449 integrated circuit has a maximum input bias current of 45 µA. While this may seem to be an insignificant value, consider that this current is drawn through resistor R_2 causing a voltage to appear at the input of the circuit which is then multiplied by the gain of the system. The result of a large value for R_2 is that an undesirable DC offset will appear at the output of the circuit. It is also important to note that at high frequencies the input impedance of this stage is:

$$R_{IN} \approx R_{IN} || R_2 = 47.6\Omega \tag{6.2}$$

This is a slight deviation from the ideal value of 50 ohms but was not found to impede the function of the output filters on the AD9854 evaluation module. The values for C_1 and C_2 were simply the largest value of ceramic and polystyrene caps found available. These two dielectric types were used because of their favorable high-frequency performance. The gain resistor R_G was calculated to produce a 1 Vrms signal at the output of this stage and its value was calculated using the equation given by Maxim:

$$A_V = \frac{1Vrms}{.160Vrms} = 1 + \frac{300}{R_G} \rightarrow R_G = 57.14\Omega \approx 56\Omega \tag{6.3}$$

6.4 Wideband Output Amplifiers

Several design requirements limit the number of parts suitable for the output amplification of this system. To start, the slew rate requirements of these components are very large. The slew rate of an amplifier is defined as the fastest rate at which the output voltage can change and is given most commonly in the units of V/μS. For a sinusoid, the maximum slew rate, which occurs at the zero crossing points, is directly related to the frequency and amplitude of the waveform:

$$R_S = 2\pi Af \tag{6.4}$$

Where A is the amplitude of the waveform and f is the frequency. For example, the required slew rate for an amplifier to produce a 5Vrms sinewave at 100 MHz is 4442.21 V/μS. By requiring a large gain, high slew rate, and high supply voltages in order to produce large voltage swings at the output, the number of suitable parts is very limited. Texas Instruments THS3092 dual current-feedback operational amplifiers were used in the output circuitry because they were able to meet the design specifications. Likewise, the THS3092 amplifier was available in an evaluation module similar to the AD9854 in order to speed prototyping. Applicable parameters of the THS3092 amplifier are displayed in Table 6.

Table 6: THS3062 Amplifier parameters.

Parameter	Value	Unit
Slew Rate	5700	V/uS
Supply Voltage	+/-15	V
Output Current	250	mA
Bandwidth (Av=1)	160	MHz

Interestingly, current-feedback amplifiers do not exhibit the direct relationship between gain and bandwidth that more typical voltage-feedback amplifiers do

Because the THS3062 is a two channel amplifier, two ICs were required to produce the necessary four output signals. Both channels of each THS3092 were configured in the wideband non-inverting configuration given in the datasheet and illustrated in Figure 32. By using the evaluation module for these components, configuring the amplifiers for wideband non-inverting operation only required replacing two surface-mount resistors on the boards. The current supplied to the inverting input of the amplifier by the feedback look is a critical parameter in determining amplifier performance, most manufacturers specify the ideal values for resistors R_F and R_G. The values displayed are those specified by Texas Instruments in order to ensure maximally flat response for a gain of 10.

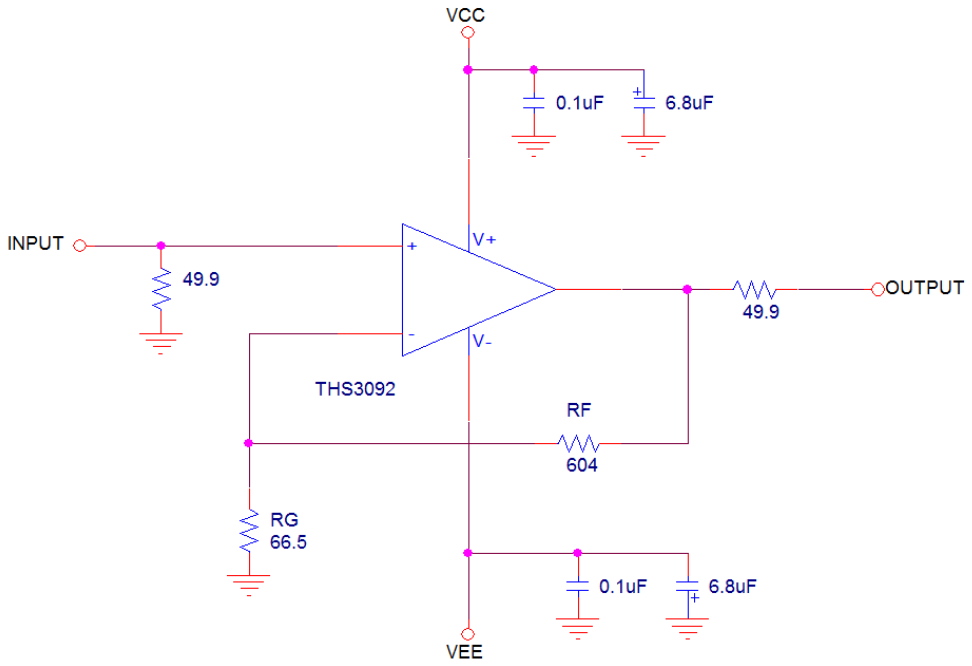

Figure 32: Wideband non-inverting configuration of the THS3092.

6.5 System Construction

The previously described electronics were mounted on a white plastic board that also contained the power supply for the system. A linear power supply was chosen to power the system in order to avoid the additional noise associated with switching topologies. The output of a transformer is first rectified and filtered before it is regulated by low-noise, low dropout linear regulators (LT1965, Linear Technology, Milpitas CA). A complete schematic of the power supply is shown in Appendix A.

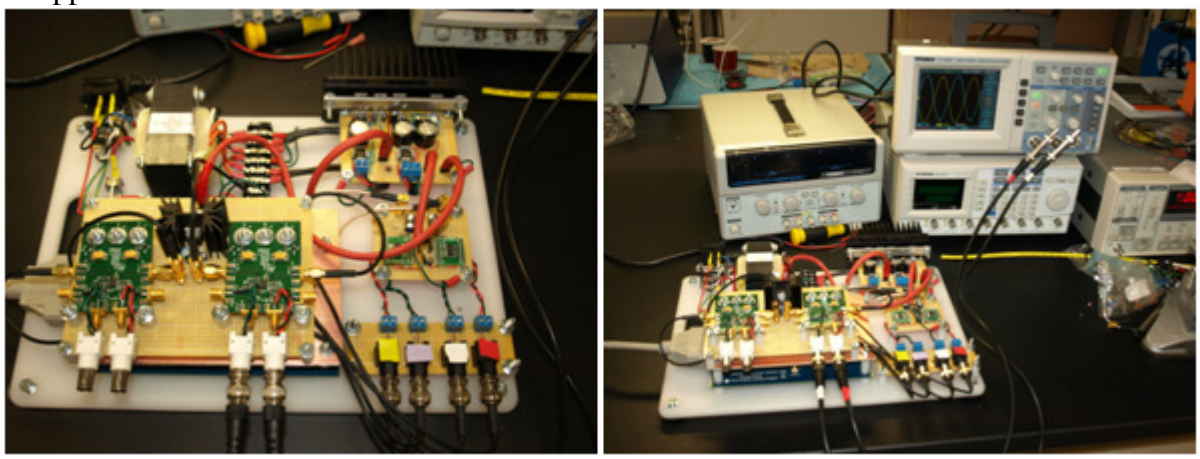

Figure 33: Prototyped quadrature signal generation system mounted on a teflon board. Using a modular approach allows the different components to be updated. (Left) All circuits were prototyped on standard perforated circuit board. (Right) Demonstration of two channel output into 50 ohms loads.

Each of the sections of the system was assembled on a separate perforated circuit board in order to allow for reconfiguring and updating of the overall system. Because a modular approach was taken, interconnections between the line-driving stage and the output amplifiers are made using a 50 ohm impedance transmission line. While this method greatly increases the flexibility of the

system, the total voltage output of the line driving stage is divided in half by the output impedance and matching impedance. Locating all the components close to each other on a dedicated printed circuit board would eliminate these losses.

6.6 System Performance

The output from two of the channels is shown in Figure 34. The maximum output of the system into a 50 ohm load is 3.75 Vp or 7.5Vpp. The bandwidth of the system and phase of the outputs were plotted over a wide frequency range using a lock-in amplifier (SR-844, Stanford Research, Palo Alto CA). Two channels were measured at a time and the signal was first attenuated using 20 dB RF attenuators in order to protect the lock-in amplifier's inputs.

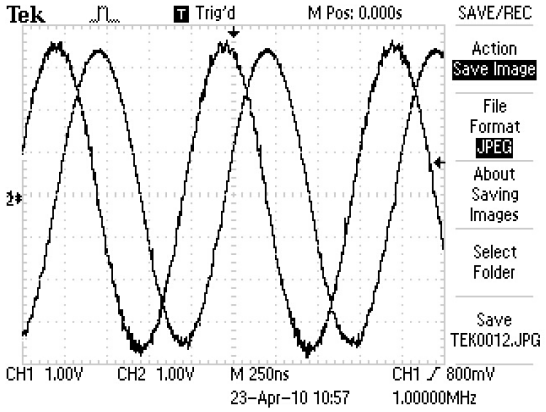

Figure 34: Output waveform of the electrorotation electronics into a 50 ohm load. The two channels show a 7.5Vpp output at 1 MHz and a 90 degree phase offset.

The output frequency response in Figure 35 was made by plotting the output voltage for 64 discrete points from 10 Hz to 100 MHz. The data below 400 kHz was acquired through direct measurement from an oscilloscope though the 20 db RF attenuators remained in the signal chain to prevent any introduction of error. As can be seen from the spectrum the output of this system is extremely linear over a very wide range of frequencies. At maximum output the -3dB points in the response occur at 17 Hz and 70 MHz. While this is impressive it should be noted that maximum output is most likely too high for electrorotation experiments and a useable voltage range can be maintained over the entire bandwidth from 10 Hz to 100 MHz.

A similar method was used to plot the phase response of the system and is shown in Figure 36. All phase measurements were made relative to the 0 degree channel at 64 discrete points between 10 Hz and 100 MHz. Again an oscilloscope was used to perform measurements below 400 kHz and these results were spliced into the data taken from the lock-in amplifer. Because measuring the time delay between two waveforms on an oscilloscope is a much less accurate measurement of phase than measurement with a lock-in amplifier, the results below 400 kHz show variation that may not be indicative of the actual performance. Even with the variability introduced by the measurement, the system shows fantastic performance with very little deviation from the ideal values of 90, 180, and 270 degrees of phase offset.

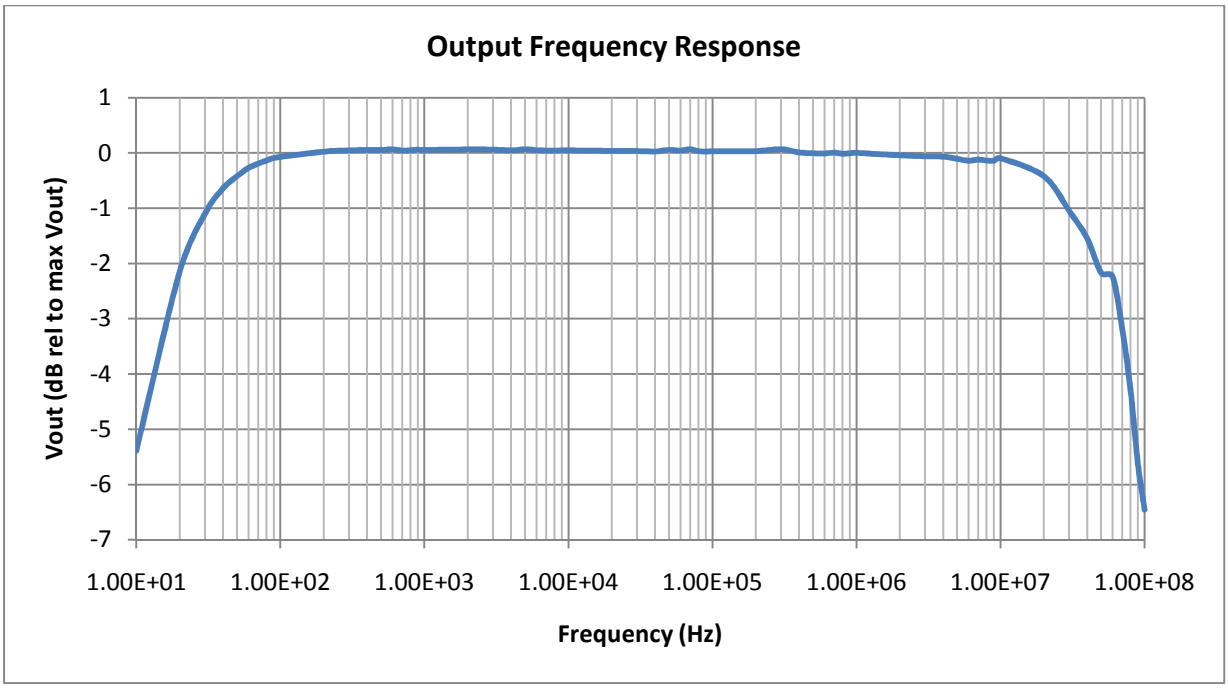

Figure 35: Amplitude response of the electrorotation electronics presented here. This spectrum was taking at maximum output of the system (7.5Vpp) and the decibel scale is relative to that voltage level. The -3dB points shown on this plot are at approximately 17 Hz and 70 MHz.

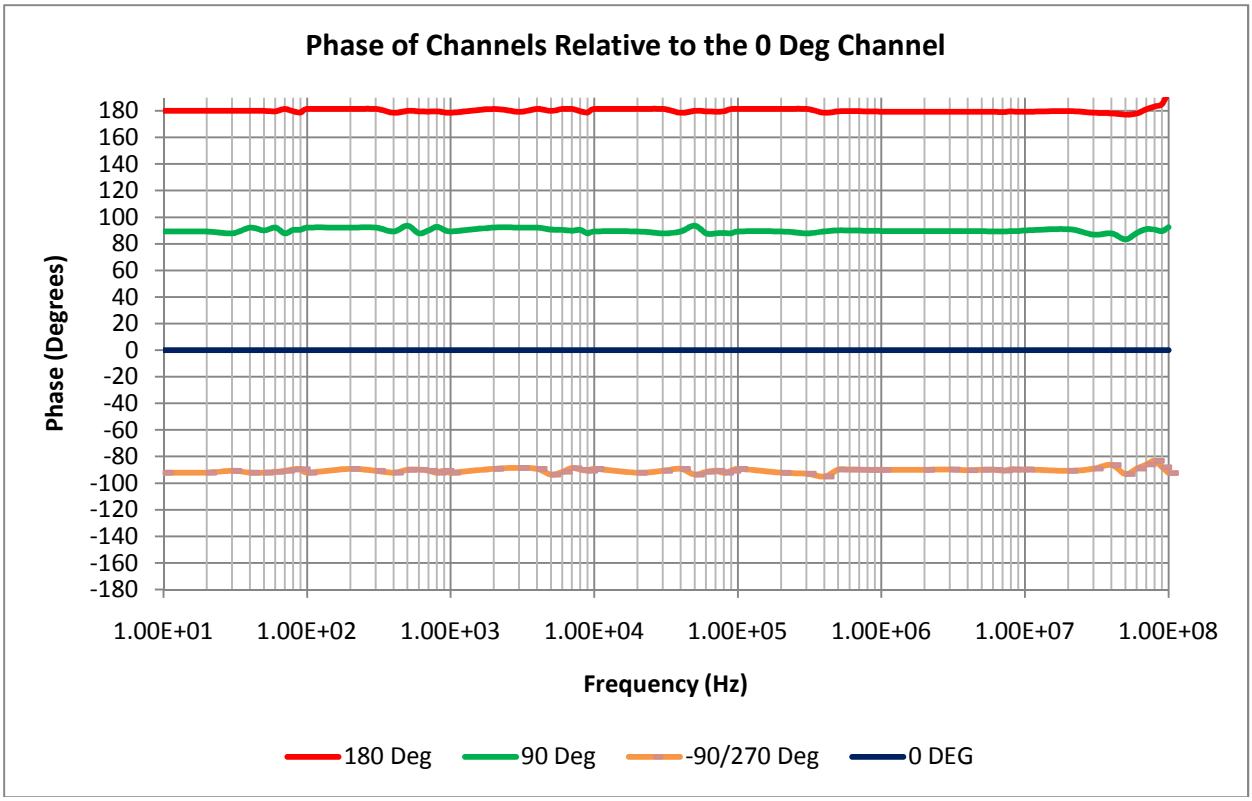

Figure 36: Phase response of all four channels measured relative to the 0 degree channel. This plot shows very little deviation from the ideal values.

6.7 Electrode Design and Fabrication

Electrorotation experiments must be performed under a microscope to facilitate the observation and measurement of cell rotation. To that end, electrodes must be fabricated on a transparent substrate that also contains the necessary connections for the four excitation signals. The electrode geometry chosen is the polynomial design described by Huang in 1991[77]. This design consists of four electrodes with parabolic ends, the peaks of which are placed in a circle or radius R= 100µm. While this design does not directly aid in electrorotation experiments it does have a benefit which is not immediately apparent. The curved nature of the electrodes produces an area at the center of all four electrodes in which DEP force is negligible (Figure 37); therefore the cell's position should not be affected.

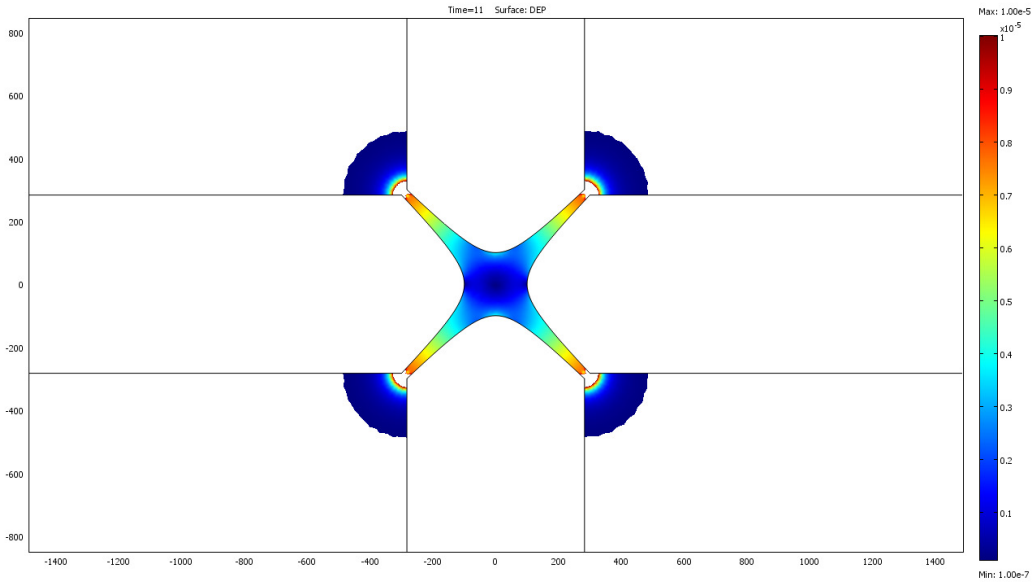

Figure 37: Finite element analysis of the gradient of the electric field within the electrode array. Notice there is a large area of negligible gradient at the center of the array.

The electrodes were fabricated on a Pyrex wafer using photolithography to pattern a photoresist spun onto the wafer. Titanium was evaporated onto the wafer as an adhesion layer between the Pyrex substrate and a layer of gold that was to serve as the electrode surface. These structures were then diced into rectangles approximately 1 inch by 1 inch. The completed electrode structure is shown in Figure 38; the distance between the opposing tips of the electrodes is 200 µm.

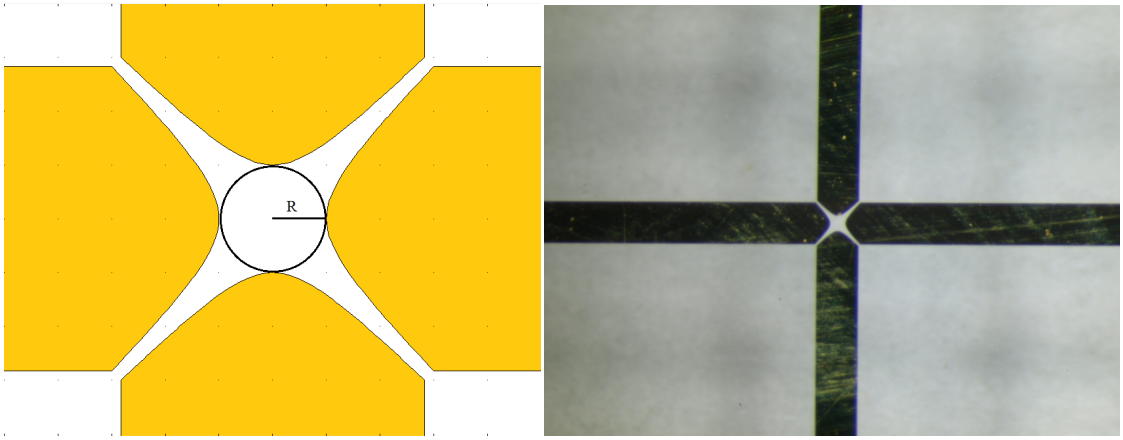

Figure 38: (Left) Electrode tip placement on a circle of 100µm. (Right) The finished gold electrodes on a pyrex wafer.

Because this apparatus is meant to be positioned on a microscope stage, it must be connected to the signal generation equipment by cables. At high frequencies the length of these cables must be considered as it approaches the wavelength of the frequency being transmitted. As a rule of thumb, transmission line effects should be considered when the length of the cable approaches one tenth of the wavelength of the transmitted signal. For our system with 1 meter coaxial cables:

$$\frac{\lambda}{10} = 1m = \frac{c}{10f} \rightarrow f = 30MHz \tag{6.5}$$

Where *f* is frequency and c is the speed of light (3×10^8 m/s). Equation 6.5 shows that for frequencies above 30 MHz, the one meter coaxial cables from the signal generation electronics act as transmissions lines so ringing effects may occur if the cables are not properly terminated. Four BNC connectors were soldered to a perforated circuit board and a 50 ohm resistor was connected from the inputs to ground. This load matching resistor prevents any load reflections from occurring. A rectangular window was cut into the perforated circuit board using a rotary tool and the diced electrode structures were epoxied into place. Connections to the gold electrodes on the glass were made by fanning out a copper wire on the electrode and attaching it to the surface using conductive silver paint (SPI Flash DRY, SPI Supplies, West Chester PA). The bond formed between the wire and the surface was then covered with a two part epoxy to prevent the silver paint from contaminating the sample. The finished electrode apparatus is shown in Figure 39.

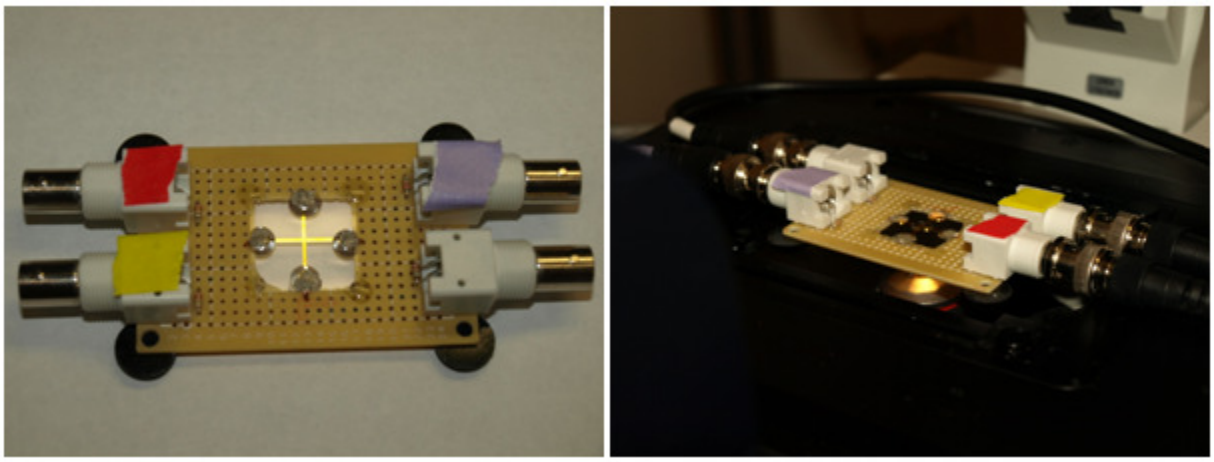

Figure 39: (Left) Completed electrode assembly featuring gold electrodes and terminated connectors for the four phase-shifted signals. (Right) The assembly is installed in the microscope stage for direct observation of the experiment.

6.8 Experimental Results

The combination of the signal generation equipment and the electrode apparatus has not been used to date to determine the rotational spectroscopy of a cell. However, qualitative examinations of electrorotation have been performed with THP-1 human leukemia cells. Experiments were performed by suspending THP-1 cells in the DEP buffer described previously and then pipetting a small amount of the solution onto the electrode array. A cover slip was then placed over the suspension and the rotating electric field was applied. Initial experiments showed that cells had a propensity to adhere to the glass substrate that the electrodes were patterned on. To alleviate this problem the surface was treated with a coating to make the Pyrex wafer highly hydrophobic and mitigate cell adhesion (Sigmacote SL2, Sigma-Aldrich Co., St. Louis, MO).

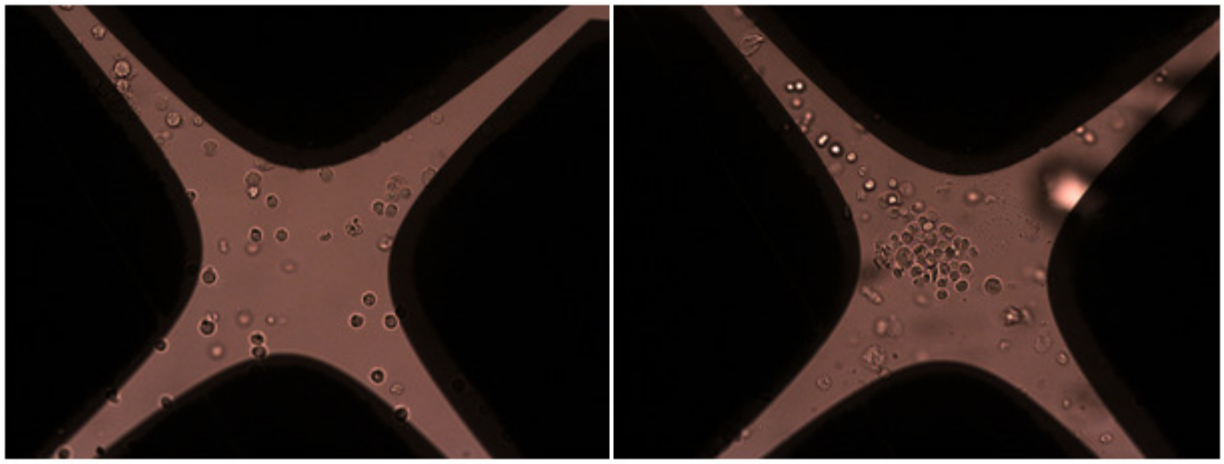

Figure 40: (Left) Random distribution of THP-1 cells around the electrode array without the application of an electric field. (Right). The application of a 3Vpp 10kHz signal to the electrode array shows the concentration of the cells in the region of low gradient of electric field.

Figure 40(Left) shows the random distribution of THP-1 human leukemia cells in the device prior to the application of an electric field. As can be seen in the image on the right, the application of a 10kHz, 3Vpp signal to the electrode array causes the cells to gather at the center of the array in an area with a low gradient of the electric field. This concentration is due to negative DEP force on the cells. Although electrorotation was observed in these preliminary experiments, the high concentration of cells made cell-cell interactions common and therefore the rotation rate of each cell was affected by the cells around it. Future electrorotation experiments should use a much lower concentration of cells to ensure accurate results.

Chapter 7: Conclusions and Future Work

7.1 Summary of Results

The work presented herein has displayed two methods for generating the high-voltage and high-frequency signals necessary for cDEP microfluidics. The first method presented was through the use of a high-voltage inverter circuit. This concept was demonstrated through the use of a Royer-oscillator type inverter circuit, intended for use in cold cathode fluorescent lamps, to illicit a DEP response from cells passing through a cDEP device. This circuit successfully demonstrated DEP trapping and pearl chaining of THP-1 and MCF-7 cells and the results were published in Biomedical Microdevices[12]. The low cost and simplicity of this method made it the ideal solution to rapidly demonstrate the cDEP concept

The second method for the generation of high-voltage and high-frequency waveforms presented was the use of a wideband amplifier and transformer combination. To illustrate this concept, a system was constructed with the direct cooperation from industry that was able to provide up to a 1000Vrms waveform at frequencies up to 1 MHz. The added flexibility of this design allowed for cDEP microfluidic devices to separate THP-1 cells from heterogeneous samples also containing polystyrene beads, and to separate live THP-1 cells from dead[13, 14]. The results were presented in papers submitted to the Journal of the Association of Laboratory Automation and Lab on a Chip.

Finally, a simple but high-performance method for the generation of the four phase-shifted sine waves necessary for electrorotation spectroscopy was presented. This method relied upon the use of a direct digital synthesis integrated circuit to perform the waveform generation. Subsequent phase splitting and amplification allowed this system to demonstrate a useable bandwidth from 10 Hz to 100 MHz at an output level of 7.5 V peak to peak. A complementary electrode apparatus was also fabricated to facilitate the direct observation of the cells in the electrode array. Qualitative observations of electrorotation have been performed in the device, and the validity of the numerical modeling was confirmed through the concentration of THP-1 human leukemia cells into a region of negligible DEP force. The measurement of accurate rotation rates was impeded however by the high concentration of cells.

7.2 Future Work

Much work remains to be done if cDEP is to be a viable alternative to current sample enrichment techniques. The two methods of signal generation presented here both have inherent advantages and disadvantages. Oscillator based signal generation systems have the advantages of low-cost, simplicity, and portability all the while maintaining the ability to produce very large output voltages. Unfortunately, for the current devices presented, these advantages come at the cost of the ability to vary experimental parameters, most notably frequency. This however is simply a limitation imposed by the current execution of the concept. The incorporation of switched passive components into the inverter circuit may allow for the frequency of oscillation to be varied over a much larger frequency range. Furthermore, by enclosing this system in a feedback loop any non-linearities in the output voltage introduced by switched components could be compensated for.

The amplifier and transformer combination system presented in this work added the ability to vary the experimental parameters over a much larger range of frequencies; giving cDEP the

opportunity to demonstrate much more advanced separations. This system also opens the possibility to integration of computer control into the system to facilitate greater automation. Indeed the future of cDEP lies in the development of a fully integrated electrical and fluidic system. However, because the current generation of cDEP devices is fabricated out of PDMS, the dielectric breakdown of the barriers separating the electrode reservoirs from the sample channel occurs at voltages far below those the transformer is capable of. Hence, it would be preferable if a high-voltage amplifier was used rather than the amplifier and transformer combination. This would eliminate the non-linearity in the output amplitude introduced by the transformer.

Referring to Figure 4, a problem with all cDEP devices becomes apparent. The problem is that for a given applied voltage, if the frequency is varied, so does the electric field intensity in the sample channel. This problem arises from the frequency dependent impedances of the barriers separating the sample channel from the electrode reservoirs. Because this introduces a variable into the experimental parameters, future electronics for cDEP may seek to maintain a constant field in the sample channel. One proposed method of doing this is by measuring the current through the system and using a feedback loop to maintain this current, and therefore the electric field, at a constant level. While in principle this may be possible, in reality this proves far more difficult. As was stated earlier, the current flow in the system is dominated by parasitic, including the capacitive coupling of the wires inserted into the electrode reservoirs. Because these parasitics depend not only on frequency, but the physical orientation of the device itself, they are impossible to predict. Thus it is not probable that direct measurement of the current flowing through the system will allow a constant field to be maintained. That being said, it is this author's theory that the current flowing through the leakages in this system will not be in phase with the current flowing through the device itself. Thus it may be possible to extract the current flowing through the device using a lock-in measurement technique.

Finally, the electronics developed here for electrorotation spectroscopy must be used to determine the dielectric properties of a cell. Through the development of a measurement and curve fitting algorithm it is hoped that ROT spectra will become a useful tool in the development of future cDEP devices. Also, it may be found that other areas of biomedical engineering research may benefit from investigation into the effects on the cell membrane. For example, electroporation treatment parameters may be optimized through the direct analysis of the cell membrane capacitance and conductance and thus its associated charging time. Also, the effect of nanoparticles and carbon nanotubes on the properties of the cell membrane, both with and without electroporation treatment can be investigated with these electronics. Because, at its heart the system is simply a computer-controlled function generator with outputs in quadrature it can form the basis for many laboratory analysis systems. Most notably is its use to perform impedance spectroscopy which can be used to related the properties of a bulk tissue to those properties of an individual cell as found through electrorotation.

References

1. Giddings, J.C., *Field-Flow Fractionation: Analysis of Macromolecular, Colloidal, and Particulate Materials.* Science, 1993. **269**: p. 1456-1465.
2. Miltenyi, S., et al., *High-Gradient Magnetic Cell-Separation with MACS.* Cytometry, 1990. **11**(2): p. 231-238.
3. Bonner, W.A., et al., *Fluorescence Activated Cell Sorting.* Review of Scientific Instruments, 1972. **43**(3): p. 404-409.
4. Agurcia, C.A., et al., *The behavioral risks and life circumstances of adolescent mothers involved with older adult partners.* Arch Pediatr Adolesc Med, 2001. **155**(7): p. 822-30.
5. Ashkin, A., J.M. Dziedzic, and T. Yamane, *Optical trapping and manipulation of single cells using infrared-laser beams.* Nature, 1987. **330**(6150): p. 769-771.
6. Pohl, H., *The Motion and Precipitation of Suspensoids in Divergent Electric Fields.* Applied Physics, 1951. **22**: p. 869-871.
7. Pohl, H., *Some Effects of Nonuniform Fields on Dielectrics.* Applied Physics, 1958. **29**: p. 1182-1188.
8. Yang, J., et al., *Cell separation on microfabricated electrodes using dielectrophoretic/gravitational field flow fractionation.* Analytical Chemistry, 1999. **71**(5): p. 911-918.
9. Gascoyne, P.R.C. and J.V. Vykoukal, *Dielectrophoretic-based sample handling in general purpose programmable diagnostic instruments.* Proceedings of the IEEE, 2004. **92**(1): p. 22-41.
10. Hughes, M., *Strategies for dielectrophoretic separation in laboratory-on-a-chip systems.* Electrophoresis, 2002. **23**(16): p. 2569-2582.
11. Steffen Hardt, F.S., *Microfluidic Technologies for Miniaturized Analysis Systems*. Book, ed. S.D. Senturia. 2007: Springer.
12. Shafiee, H., et al., *Contactless Dielectrophoresis: A New Technique For Cell Manipulation.* Biomedical Microdevices, 2009.
13. Shafiee, H., et al., *Selective isolation of live/dead cells using contactless dielectrophoresis (cDEP).* Lab on a Chip, 2010. **10**(4): p. 438-445.
14. Shafiee, H., J.L. Caldwell, and R.V. Davalos, *A Microfluidic System for Biological Particle Enrichment Using Contactless Dielectrophoresis.* Journal of the Association for Laboratory Automation, 2010. **15**(3): p. 224-232.
15. Theron, J., et al., *Detection of toxigenic Vibrio cholerae from environmental water samples by an enrichment broth cultivation-pit-stop semi-nested PCR procedure.* Journal of Applied Microbiology, 2000. **89**(3): p. 539-546.
16. Lazcka, O., F.J. Del Campo, and F.X. Munoz, *Pathogen detection: A perspective of traditional methods and biosensors.* Biosensors & Bioelectronics, 2007. **22**(7): p. 1205-1217.
17. Stevens, K.A. and L.A. Jaykus, *Bacterial separation and concentration from complex sample matrices: A review.* Critical Reviews in Microbiology, 2004. **30**(1): p. 7-24.
18. Stevens, M.M. and J.H. George, *Exploring and engineering the cell surface interface.* Science, 2005. **310**(5751): p. 1135-1138.
19. Uusijärvi, J., B. Egestad, and J. Sjövall, *Manual and automated enrichment procedures for biological samples using lipophilic gels.* Journal of Chromatography B: Biomedical Sciences and Applications, 1989. **488**(1): p. 87-104.

20. Lindqvist, R., *Preparation of PCR samples from food by a rapid and simple centrifugation technique evaluated by detection of Escherichia coli O157:H7.* International Journal of Food Microbiology, 1997. **37**(1): p. 73-82.
21. Chang, W.C., L.P. Lee, and D. Liepmann, *Biomimetic technique for adhesion-based collection and separation of cells in a microfluidic channel.* Lab Chip, 2005. **5**(1): p. 64-73.
22. Laplace-Builhé, C., et al., *Application of flow cytometry to rapid microbial analysis in food and drinks industries.* Biology of the Cell, 1993. **78**(1-2): p. 123-128.
23. Ueckert, J., et al., *Flow cytometry applications in physiological study and detection of foodborne microorganisms.* International Journal of Food Microbiology, 1995. **28**(2): p. 317-326.
24. Cudjoe, K.S., R. Krona, and E. Olsen, *IMS: a new selective enrichment technique for detection of Salmonella in foods.* International Journal of Food Microbiology, 1994. **23**(2): p. 159-165.
25. Fu, A.Y., et al., *A microfabricated fluorescence-activated cell sorter.* Nat Biotechnol, 1999. **17**(11): p. 1109-11.
26. Pohl, H., *Dielectrophoresis*. 1978, Cambridge: Cambridge University Press.
27. Pohl, H. and J. Crane, *Dielectrophoresis of Cells.* Biophysical Journal, 1971. **11**(9): p. 711-727.
28. Pohl, H., *Dielectrophoresis.* Cambridge University Press: Cambridge, 1978., 1978.
29. Pohl, H.A., *Some Effects of Nonuniform Fields on Dielectrics.* J. Appl. Phys. , 1958. **29**.
30. Hughes, M.P., *Strategies for dielectrophoretic separation in laboratory-on-a-chip systems.* Electrophoresis, 2002. **23**(16): p. 2569-2582.
31. Yang, J., et al., *Cell separation on microfabricated electrodes using dielectrophoretic/gravitational field flow fractionation.* Analytical Chemistry, 1999. **71**(5): p. 911-918.
32. Becker, F.F., et al., *The removal of human leukaemia cells from blood using interdigitated microelectrodes.* J. Phys. D: Appl. Phys., 1994. **27**: p. 2659-2662.
33. Gascoyne, P.R.C., et al., *Dielectrophoretic separation of cancer cells from blood.* IEEE Transactions on Industry Applications Annual Meeting of the Industry-Applications-Society, 1997. **33**(3): p. 670-678.
34. Huang, Y., et al., *Dielectrophoretic cell separation and gene expression profiling on microelectronic chip arrays.* Anal Chem, 2002. **74**(14): p. 3362-71.
35. Cheng, J., et al., *Preparation and hybridization analysis of DNA/RNA from E. coli on microfabricated bioelectronic chips.* Nat Biotechnol, 1998. **16**(6): p. 541-6.
36. Altomare, L., et al., *Levitation and movement of human tumor cells using a printed circuit board device based on software-controlled dielectrophoresis.* Biotechnology and Bioengineering, 2003. **82**(4): p. 474-479.
37. Markx, G.H., et al., *Dielectrophoretic characterization and separation of microorganisms.* Microbiology-UK, 1994. **140**: p. 585-591.
38. Das, C.M., et al., *Dielectrophoretic segregation of different human cell types on microscope slides.* Anal Chem, 2005. **77**(9): p. 2708-19.
39. Gambari, R., et al., *Applications to cancer research of "lab-on-a-chip" devices based on dielectrophoresis (DEP).* Technology in Cancer Research & Treatment, 2003. **2**(1): p. 31-39.

40. Becker, F., et al., *The removal of human leukaemia cells from blood using interdigitated microelectrodes.* J. Phys. D: Appl. Phys, 1994. **27**: p. 2659-2662.
41. Gascoyne, P., et al., *Dielectrophoretic Separation of Cancer Cells from Blood.* IEEE Trans. Industry Applications, 1997. **33**: p. 670-678.
42. Huang, Y., et al., *Dielectrophoretic cell separation and gene expression profiling on microelectronic chip arrays.* Anal Chem, 2002. **74**: p. 3362-3371.
43. Cheng, J., et al., *Preparation and hybridization analysis of DNA/RNA from E. coli on microfabricated bioelectronic chips.* Nat Biotechnol, 1998. **16**: p. 541-546.
44. Stephens, M., et al., *The dielectrophoresis enrichment of CD34+ cells from peripheral blood stem cell harvests.* Bone Marrow TRansplant, 1996. **18**: p. 777-782.
45. Huang, Y., et al., *Introducing dielectrophoresis as a new force field for field-flow fractionation.* Biophys J, 1997. **73**: p. 1118-1129.
46. Kim, U.-J., et al., *Selection of mammalian cells based on their cell-cycle phase using dielectrophoresis.* Proc Natl Acad Sci, 2007. **104**: p. 20708-20712.
47. Masuda, S., T. Itagaki, and M. Kosakada, *Detection of extremely small particles in the nanometer and ionic size range.* Ieee Transactions on Industry Applications, 1988. **24**(4): p. 740-744.
48. Chou, C., et al., *Electrodeless dielectrophoresis of single- and double-stranded DNA.* Biophysical Journal, 2002. **83**(4): p. 2170-2179.
49. Davalos, R.V., et al., *Performance impact of dynamic surface coatings on polymeric insulator-based dielectrophoretic particle separators.* Analytical and Bioanalytical Chemistry, 2008. **390**(3): p. 847-855.
50. Blake A. Simmons, G.J.M., Rafael V.Davalos, Gregory J. Fiechtner, Yolanda Fintschenko, and Eric B. Cummings, *The Development of Polymeric Devices as Dielectrophoretic Separators and Concentrators.* MRS BULETIN, 2006. **31**.
51. Lapizco-Encinas, B.H., et al., *An insulator-based (electrodeless) dielectrophoretic concentrator for microbes in water.* Journal of Microbiological Methods, 2005. **62**(3): p. 317-326.
52. Lapizco-Encinas, B.H., et al., *Insulator-based dielectrophoresis for the selective concentration and separation of live bacteria in water.* Electrophoresis, 2004. **25**(10-11): p. 1695-704.
53. Sabounchi, P., et al., *Sample concentration and impedance detection on a microfluidic polymer chip.* Biomedical Microdevices, 2008. **10**(5): p. 661-670.
54. Lapizco-Encinas, B.H., S. Ozuna-Chacon, and M. Rito-Palomares, *Protein manipulation with insulator-based dielectrophoresis and direct current electric fields.* J Chromatogr A, 2008. **1206**(1): p. 45-51.
55. Cummings, E.B. and A. Singh, *Dielectrophoresis in Microchips Containing Arrays of Insulating Posts: Theoretical and Experimental Results.* Analytical Chemistry, 2003. **75**: p. 4724-4731.
56. Sabounchi, P., et al. *Joule Heating Effects on Insulator-based Dielectrophoresis*. in *Twelfth International Conference on Miniaturized Systems for Chemistry and Life Sciences*. 2008. San Diego, California, USA.
57. Arnold, W.M. and U. Zimmermann, *Rotation of an isolated cell in a rotating electric-field.* Naturwissenschaften, 1982. **69**(6): p. 297-298.

58. Arnold, W.M. and U. Zimmermann, *Rotating-field-induced rotation and measurement of the membrane capacitance of single mesophyll-cells of avena-sativa.* Zeitschrift Fur Naturforschung Section C-a Journal of Biosciences, 1982. **37**(10): p. 908-915.
59. Glaser, R., G. Fuhr, and J. Gimsa, *Rotation of erythrocytes, plant-cells, and protoplasts in an outside rotating electric-field.* Studia Biophysica, 1983. **96**(1): p. 11-20.
60. Lovelace, R.V.E., D.G. Stout, and P.L. Steponkus, *Protoplast rotation in a rotating electric-field - the influence of cold-acclimation.* Journal of Membrane Biology, 1984. **82**(2): p. 157-166.
61. Arnold, W.M. and U. Zimmermann, *Electro-rotation - development of a technique for dielectric measurements on individual cells and particles.* Journal of Electrostatics, 1988. **21**(2-3): p. 151-191.
62. Fuhr, G. and P.I. Kuzmin, *Behavior of cells in rotating electric-fields with account to surface-charges and cell structures.* Biophysical Journal, 1986. **50**(5): p. 789-795.
63. Pastushenko, V.P., P.I. Kuzmin, and Y.A. Chizmadzhev, *Dielectrophoresis and electrorotation of cells - unified theory for spherically symmetric cells with arbitrary structure of membrane.* Biologicheskie Membrany, 1988. **5**(1): p. 65-78.
64. Chan, K.L., et al., *Electrorotation of liposomes: verification of dielectric multi-shell model for cells.* Biochimica Et Biophysica Acta-Lipids and Lipid Metabolism, 1997. **1349**(2): p. 182-196.
65. Long, Q. and W. Xing, *Detection of the apoptosis of Jurkat cell using an electrorotation chip.* Frontiers of Biology in China, 2006. **1**(2): p. 208-212.
66. Cristofanilli, M., et al., *Automated electrorotation to reveal dielectric variations related to HER-2/neu overexpression in MCF-7 sublines.* Clinical Cancer Research, 2002. **8**(2): p. 615-619.
67. Hoelzel, R., *Electrorotation of single yeast cells at frequencies between 100 Hz and 1.6 GHz.* Biophysical Journal, 1997. **73**(2): p. 1103-1109.
68. Georgieva, R., et al., *Low frequency electrorotation of fixed red blood cells.* Biophysical Journal, 1998. **74**(4): p. 2114-2120.
69. Gascoyne, P.R.C., F.F. Becker, and X.B. Wang, *Numerical analysis of the influence of experimental conditions on the accuracy of dielectric parameters derived from electrorotation measurements.* Bioelectrochemistry and Bioenergetics, 1995. **36**(2): p. 115-125.
70. Yang, J., et al., *Dielectric Properties of Human Leukocyte Subpopulations Determined by Electrorotation as a Cell Separation Criterion.* Biophysical Journal, 1999. **76**(6): p. 3307-3314.
71. Jones, T.B., *Basic theory of dielectrophoresis and electrorotation.* IEEE Eng Med Biol Mag, 2003. **22**(6): p. 33-42.
72. Morgan, H., et al., *Single cell dielectric spectroscopy.* Journal of Physics D-Applied Physics, 2007. **40**(1): p. 61-70.
73. Chan, K.L., et al., *Measurements of the dielectric properties of peripheral blood mononuclear cells and trophoblast cells using AC electrokinetic techniques.* Biochimica Et Biophysica Acta-Molecular Basis of Disease, 2000. **1500**(3): p. 313-322.
74. Huang, Y., et al., *Differences in the ac electrodynamics of viable and non-viable yeast cells determined through combined dielectrophoresis and electrorotation studies.* Physics in Medicine and Biology, 1992. **37**(7): p. 1499-1517.

75. Archer, S., H. Morgan, and F.J. Rixon, *Electrorotation studies of baby hamster kidney fibroblasts infected with herpes simplex virus type 1.* Biophysical Journal, 1999. **76**(5): p. 2833-2842.
76. Chadderton, N., *Transistor Considerations for LCD Backlighting.* Zetex Application Note, 1996. **14**(2): p. 12.
77. Huang, Y. and R. Pethig, *Electrode design for negative dielectrophoresis.* Measurement Science & Technology, 1991. **2**(12): p. 1142-1146.

Appendix A: Electrorotation Electronics Power Supply

Schematic of power supply used for the electrorotation signal generation electronics.